

# 1 Insights into Nd<sup>III</sup> to Yb<sup>III</sup> Energy Transfer and Its Implications in 2 Luminescence Thermometry

3 Mariangela Oggianu,<sup>▽</sup> Valentina Mameli,<sup>▽</sup> Miguel A. Hernández-Rodríguez,<sup>▽</sup> Noemi Monni,  
4 Manuel Souto, Carlos D.S. Brites, Carla Cannas, Fabio Manna, Francesco Quochi, Enzo Cadoni,  
5 Norberto Masciocchi, Albano N. Carneiro Neto,\* Luíís D. Carlos,\* and Maria Laura Mercuri\*



Cite This: <https://doi.org/10.1021/acs.chemmater.4c00362>



Read Online

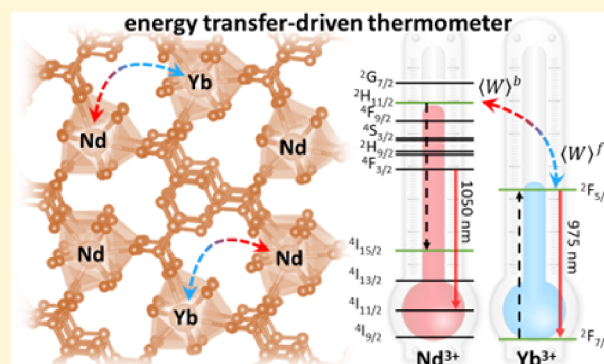
ACCESS |

 Metrics & More

 Article Recommendations

 Supporting Information

6 **ABSTRACT:** This work challenges the conventional approach of  
7 using Nd<sup>III</sup> <sup>4</sup>F<sub>3/2</sub> lifetime changes for evaluating the experimental Nd<sup>III</sup>  
8 → Yb<sup>III</sup> energy transfer rate and efficiency. Using near-infrared (NIR)  
9 emitting Nd:Yb mixed-metal coordination polymers (CPs), synthe-  
10 sized via solvent-free thermal grinding, we demonstrate that the Nd<sup>III</sup>  
11 [<sup>2</sup>H<sub>11/2</sub> → <sup>4</sup>I<sub>15/2</sub>] → Yb<sup>III</sup> [<sup>2</sup>F<sub>7/2</sub> → <sup>2</sup>F<sub>5/2</sub>] pathway, previously  
12 overlooked, dominates energy transfer due to superior energy  
13 resonance and *J*-level selection rule compatibility. This finding upends  
14 the conventional focus on the Nd<sup>III</sup> [<sup>4</sup>F<sub>3/2</sub> → <sup>4</sup>I<sub>11/2</sub>] → Yb<sup>III</sup> [<sup>2</sup>F<sub>7/2</sub> →  
15 <sup>2</sup>F<sub>5/2</sub>] transition pathway. We characterized Nd<sub>0.890</sub>Yb<sub>0.110</sub>(BTC)-  
16 (H<sub>2</sub>O)<sub>6</sub> as a promising cryogenic NIR thermometry system and  
17 employed our novel energy transfer understanding to perform  
18 simulations, yielding theoretical thermometric parameters and  
19 sensitivities for diverse Nd:Yb ratios. Strikingly, experimental thermometric data closely matched the theoretical predictions,  
20 validating our revised model. This novel perspective on Nd<sup>III</sup> → Yb<sup>III</sup> energy transfer holds general applicability for the Nd<sup>III</sup>/Yb<sup>III</sup>  
21 pair, unveiling an important spectroscopic feature with broad implications for energy transfer-driven materials design.



## 22 ■ INTRODUCTION

23 Temperature is a critical physical parameter and its accurate  
24 detection is of paramount importance in many research fields  
25 ranging from climate, metrology, aerospace, nanomedicine,  
26 production plants, and food storage.<sup>1,2</sup> During the past decade,  
27 novel temperature sensors have emerged that have the  
28 potential to substitute resistance thermometry.<sup>3</sup> All examples  
29 are based on temperature-induced changes in the material's  
30 chemical and physical properties, such as volume, electrical  
31 conductivity, or photoluminescence.

32 Among these is luminescence thermometry, which was  
33 developed as a remote temperature sensing technique that  
34 relies on the temperature dependency of luminescence features  
35 (e.g., band shape, peak energy or intensity, and excited state  
36 lifetimes and risetimes) of a phosphor to measure temper-  
37 ature.<sup>4–8</sup> This technique provides precise thermal readouts  
38 with superior spatial resolution in short acquisition times.  
39 Noticeably, luminescent thermometers can operate in distinct  
40 temperature regions, from cryogenic temperatures (<100 K),  
41 of interest in cryobiology, aerospace, nuclear fusion, and the  
42 development of superconducting magnets,<sup>9–13</sup> to high temper-  
43 atures (>400 K) with potential applications in heavy  
44 industry,<sup>14</sup> covering also the so-called physiological temper-  
45 ature range (298–323 K), of interest in biomedicine.<sup>15</sup>

Up to now, a plethora of luminescent materials, such as 46  
47 quantum dots, organic dyes, lanthanide-doped nanoparticles,  
48 and lanthanide complexes have been largely investigated for  
49 luminescence thermometry.<sup>5</sup> Among them, trivalent lanthanide  
50 (Ln<sup>III</sup>) ions, including chelate complexes,<sup>16,17</sup> polymers,<sup>18,19</sup>  
51 metal–organic frameworks (MOFs),<sup>20,21</sup> and organic–inor-  
52 ganic hybrids molecular probes,<sup>22,23</sup> are promising materials for  
53 thermal sensing, given their typical long lifetimes (10<sup>–3</sup> s  
54 range), characteristic sharp emission, and high emission  
55 quantum yields, emitting in the ultraviolet, visible, and near-  
56 infrared spectral regions.<sup>17,24,25</sup>

It is well-known that Ln<sup>III</sup> centers cannot efficiently absorb 57  
58 light due to forbidden 4*f*–4*f* transitions.<sup>26</sup> To overcome this, a  
59 challenging strategy for the fabrication of highly performant  
60 Ln-based materials, including luminescent thermometers, lies  
61 in the incorporation of luminescent linkers as a suitable  
62 antenna, thereby being able to absorb and transfer energy to  
63 the Ln<sup>III</sup> centers.<sup>27</sup> Lanthanide-based coordination polymers

Received: February 8, 2024

Revised: March 12, 2024

Accepted: March 13, 2024

64 (CPs) and MOFs are excellent candidates for optical sensors  
65 due to their ability to show both ligand-centered and metal-  
66 centered luminescence. The proper choice of the luminescent  
67 building blocks, both Ln<sup>III</sup> ions (metallic nodes) and functional  
68 organic linkers, is crucial to designing new CPs for thermal  
69 sensing applications showing different pathways of energy  
70 exchange, including intensity-based and ratiometric thermom-  
71 eters.<sup>28</sup>

72 Recently, mixed Ln'Ln"-MOFs thermometers have been  
73 developed where the intensity ratio of two emissions from  
74 different lanthanide ions, commonly Tb<sup>III</sup> and Eu<sup>III</sup>, is used as  
75 the thermometric parameter,<sup>20,21,29,30</sup> based on emissions in  
76 the visible spectral range. Cui et al. reported on the first  
77 example of a luminescent thermometer, based on mixed-Eu<sup>III</sup>/  
78 Tb<sup>III</sup> MOF and Eu<sub>0.0069</sub>Tb<sub>0.9931</sub>-DMBDC (DMBDC = 2,5-  
79 dimethoxy-1,4-benzene-dicarboxylate), showing a significant  
80 temperature-dependent photoluminescence in the 10–300 K  
81 range.<sup>20</sup> Besides the Eu<sup>III</sup>/Tb<sup>III</sup> pair, the Nd<sup>III</sup> and Yb<sup>III</sup> ions  
82 have been receiving growing interest given their harmless  
83 emission wavelength and deep penetration length in biological  
84 tissues.<sup>31–38</sup> However, all of the works reported so far rely on  
85 an unpredictable serendipitous approach, lacking a compre-  
86 hensive elucidation of the thermometric performance rooted in  
87 donor-to-acceptor energy transfer mechanisms between Ln<sup>III</sup>  
88 ions. This absence of understanding hinders the rational  
89 optimization of these materials.

90 Therefore, in this study, we employ a novel class of NIR-  
91 emitting Yb/Nd CPs based on the 1,3,5-benzentricarboxylic  
92 acid (H<sub>3</sub>BTC) organic linker to deeply investigate the Nd–Yb  
93 energy transfer process and quantitatively illustrate its  
94 influence on the thermometric properties of the materials.  
95 Then, the objective of the manuscript is to fully understand the  
96 underlying energy transfer mechanisms, and their crucial  
97 implications for optimizing energy transfer-driven ratiometric  
98 luminescent thermometers, rather than looking for a higher  
99 thermometric performance. Two different classes have been  
100 synthesized through a solvent-free thermal grinding method,  
101 formulated as Nd<sub>x</sub>Yb<sub>(1-x)</sub>(BTC)(H<sub>2</sub>O)<sub>6</sub> ( $x = 1$  (1);  $x = 0.943$   
102 (2);  $x = 0.953$  (3);  $x = 0.890$  (4)) and Nd<sub>x</sub>Yb<sub>(1-x)</sub>(BTC) ( $x =$   
103 0.017 (5),  $x = 0$  (6)). Single lanthanide Nd-CPs and Yb-CPs  
104 have also been prepared as reference samples. The obtained  
105 materials have been morphologically, structurally, and  
106 thermally characterized and their photophysical processes  
107 (10–300 K) have been studied to determine the temperature  
108 dependence of the Nd<sup>III</sup>-to-Yb<sup>III</sup> energy transfer processes in a  
109 representative sample, Nd<sub>0.890</sub>Yb<sub>0.110</sub>(BTC)(H<sub>2</sub>O)<sub>6</sub> (4) using  
110 the Nd-BTC (1) as a reference.

111 We demonstrate, both from experimental measurements and  
112 theoretical calculations, that the experimental Ln-to-Ln energy  
113 transfer rate ( $W_{\text{exp}}$ )<sup>39</sup>

$$114 \quad W_{\text{exp}} = \frac{1}{\tau_{\text{DA}}} - \frac{1}{\tau_{\text{D}}} \quad (1)$$

115 and the energy transfer efficiency ( $\eta_{\text{ET}}$ )<sup>40,41</sup>

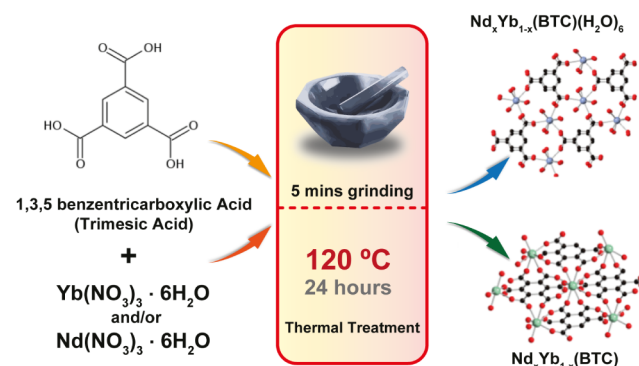
$$116 \quad \eta_{\text{ET}} = 1 - \frac{\tau_{\text{DA}}}{\tau_{\text{D}}} \quad (2)$$

117 ( $\tau_{\text{D}}$  and  $\tau_{\text{DA}}$  are the lifetimes of the emitting level of the  
118 donor in the absence and presence of acceptors, respectively)  
119 are not valid for the specific case of Nd<sup>III</sup>–Yb<sup>III</sup> energy transfer  
120 when Nd<sup>III</sup>  $^4\text{F}_{3/2} \rightarrow ^4\text{I}_{11/2}$  emission lifetimes are monitored for  
121 Nd(BTC)(H<sub>2</sub>O)<sub>6</sub> ( $\tau_{\text{D}}$ ) and Nd<sub>x</sub>Yb<sub>(1-x)</sub>(BTC)(H<sub>2</sub>O)<sub>6</sub> ( $\tau_{\text{DA}}$ )

CPs. We can anticipate that the reason behind this is that the  
122  $^4\text{F}_{3/2} \rightarrow ^4\text{I}_{11/2}$  is not an effective pathway in the Nd<sup>III</sup>–Yb<sup>III</sup>  
123 energy transfer process as other Nd<sup>III</sup> transitions (e.g.,  $^2\text{H}_{11/2}$   
124  $\rightarrow ^4\text{I}_{15/2}$ ) are responsible for the energy transfer process. Thus,  
125 a new point of view regarding the Nd<sup>III</sup>–Yb<sup>III</sup> energy transfer  
126 for excitation energies not being resonant with the  $^4\text{F}_{3/2}$  energy  
127 level is herein pointed out, contrary to what is reported in the  
128 literature.<sup>40,42–47</sup> 129

**Experimental Results and Discussion.** *Synthesis.* NIR  
130 emitter-based Ln'Ln"-CPs-CPs were synthesized through a  
131 solvent-free grinding method. Ln(NO<sub>3</sub>)<sub>3</sub>·6(H<sub>2</sub>O) (Ln<sup>III</sup> = Yb,  
132 Nd) and 1,3,5-benzentricarboxylic acid (H<sub>3</sub>BTC, trimesic  
133 acid) were mixed in a 1:1 ratio and ground for 5 min, and then  
134 thermally treated at 120 °C for 24 h, exploiting both  
135 mechanical and thermal energies (Scheme 1). This method,  
136 s1

### Scheme 1. Schematic Representation of the Thermal Grinding Process



as reported by Liu et al.,<sup>48</sup> offers a valid alternative for rapid,  
137 eco-friendly, and large-scale preparation of luminescent Ln-  
138 CPs/MOFs, avoiding the production of a large amount of  
139 solvent waste. 140

By adding to the precursor mixture a second Ln<sup>III</sup> ion, with  
141 molar ratio in the 5 to 20%, compounds formulated as  
142 Nd<sub>x</sub>Yb<sub>(1-x)</sub>(BTC)(H<sub>2</sub>O)<sub>6</sub> ( $x = 1$  (1);  $x = 0.943$  (2);  $x = 0.953$   
143 (3);  $x = 0.890$  (4)) and Nd<sub>x</sub>Yb<sub>(1-x)</sub>BTC ( $x = 0.017$  (5),  $x = 0$   
144 (6)) are obtained in the form of microcrystalline powder. 145

The materials have been fully characterized by powder X-ray  
146 diffractometry (PXRD) and Fourier transform infrared spec-  
147 troscopy (FT-IR), induced coupled plasma mass spectrometry  
148 (ICP-MS), scanning electron microscopy–energy dispersive  
149 X-ray (SEM-EDX) and thermal gravimetric analysis (TGA). 150

The synthetic process was monitored by PXRD, as shown in  
151 Figure S1 for the formation of Yb(BTC). When the precursors  
152 of 6 [H<sub>3</sub>BTC acid and Yb(NO<sub>3</sub>)<sub>3</sub>·6(H<sub>2</sub>O)] are mixed and  
153 milled for 30 s in an agate mortar, no formation of new  
154 compounds was detected. However, just after 1 min of milling,  
155 most of the precursor's diffraction peaks disappeared, and a few  
156 barely visible peaks, attributed to residual trimesic acid,  
157 remained. For longer milling times (3 to 5 min), a sort of  
158 amorphization process occurred, confirming the hypothesis  
159 originally provided by Liu et al.;<sup>48</sup> diffraction peaks  
160 progressively disappear, and the background level increases  
161 and becomes nonmonotonic. At this stage, the milled powders  
162 turned into a slurry. Treating this slurry at 120 °C led, after  
163 water elimination, to the formation of the desired Yb(BTC)  
164 CP. To verify if the grinding step had a direct role in the  
165 formation of Yb(BTC), the pristine mixture was also thermally  
166 treated, skipping the milling step. The PXRD analysis (see  
167

Figure S1) showed the obtainment of unknown crystal phases together with some residual reactants. Thus, the residual water present in the slurry could favor the reaction, as liquid-assisted grinding is used to facilitate mechanochemical reactions in disparate fields.<sup>49–51</sup> Finally, the addition of a washing step by water and then ethanol allowed for purification of the product in the case of residues of the precursor mixture.

**Crystal Structures.** Compounds 1–6 are obtained as microcrystalline powders only, hence, to determine their crystal structure, we resorted to PXRD (performed on 1 and 6 samples only), due to the isomorphous character of species 1 to 4 and, separately, 5 and 6. Compound 1 crystallizes in the monoclinic space group *Cc*, as a neutral polymeric framework, isostructural with a previously reported Gd<sup>III</sup>-based species.<sup>52</sup> The asymmetric unit of 1, shown in Figure 1A, consists of one

Nd<sup>III</sup> ion, one fully deprotonated BTC unit, and six water molecules, all bound to the rare earth cation. Each metal ion is *ennea*-coordinated, surrounded by nine oxygen atoms, three from (three different) BTC linkers and six from water molecules, leading to the Nd(BTC)(H<sub>2</sub>O)<sub>6</sub> formulation. The Nd<sup>III</sup> ions, linked through BTC ligands, form parallel 1D ribbons running along the *b* axis, as reported in Figure 1B. The stacking of these ribbons interconnected through a bevy of hydrogen bonds involving the H atoms of the coordinating water molecules, leads to a dense 3D framework (Figure 1C).

Figure 1D,E depicts the *ennea*-coordinated Nd atoms as green polyhedra and dashed red contacts indicate the rich 3D framework of hydrogen bonding, interlinking the different coordination spheres: the Nd–O bond distances are reported in Table S1. Note that, as restraints were introduced in the final Rietveld refinement cycles to stabilize the otherwise untreatable refinement diverging to an unphysical model, the obtained values mostly mirrored the numerical limits imposed of the Nd–O distances rather than their true similarity, or their dispersion.

Thermogravimetric analysis showed that all six coordinated water molecules can be completely removed by heating 1, the hexahydrate Nd(BTC)(H<sub>2</sub>O)<sub>6</sub> phase, at 130 °C (*vide infra*), leading to an amorphous material. The anhydrous Yb(BTC) (6) crystallizes as a complex 3D framework in the trigonal *R3c* space group. Its asymmetric unit consists of (a fraction of) one Yb<sup>III</sup> ion and 1/6 of the fully deprotonated BTC ligand (both lying on special positions of -3-point symmetry). The coordination sphere of each metal ion is composed of six oxygen atoms belonging to six distinct BTC linkers with a Yb–O bond distance of 2.259(3) Å, which, in turn, coordinate six Yb<sup>III</sup> ions in the  $\mu_6$  bridging coordination mode (Figure 1F).

This generates a 3D CP, where BTC aromatic rings, orderly stacked along *c* (Figure 1G), show intercalated Yb<sup>III</sup> ions located midway at a distance of 1.56 Å (*c*/12) from the virtual plane containing the neighboring (and coordinating) BTC moieties. Indeed, when 6 is observed in the *ac* plane, as shown in Figure 1H, it is evident how all the Yb<sup>III</sup> ions lay on a different, but parallel, plane than BTC linkers, forming a dense structure with no accessible cavities, with nonbonding Yb<sup>III</sup>...Yb<sup>III</sup> distances of 6.00 (out of plane) and 8.88 Å (in plane), heavily minimizing Coulombic repulsion.

In line with the structural model presented here, thermogravimetric analysis confirmed the anhydrous character of 6 (*vide infra*). The PXRD analysis (Figure 2) confirmed the obtainment of two different structures (*vide supra*), depending on the *x* content: the Nd-rich samples (2–4) feature the structure of the hydrated Nd(BTC)(H<sub>2</sub>O)<sub>6</sub>-CP (1), whereas the Yb-rich samples 5 and 6 are anhydrous and isostructural. Other intermediate substitution ratios (Nd:Yb 50:50 and 30:70) were also tested (Figure S2), but PXRD revealed the formation of polyphasic mixtures where hydrated and anhydrous phases coexist. Thus, it appears that Nd<sup>III</sup> and Yb<sup>III</sup> act as structure-directing agents for the hydrated and anhydrous phases, respectively, if they dominate in the precursor's mixture.

The results from our complete PXRD analysis also include an estimate of the specific surface areas (SSA) of our materials. As derived by the numerical analysis described in Text S1, SSA values fall well below 100 m<sup>2</sup>·g<sup>-1</sup> (in line with the experimental BET values reported in the Experimental section). Note that porous materials possess much larger SSA values (in m<sup>2</sup>·g<sup>-1</sup>, 300–5000 for activated carbons, 1000 for zeolites, and up to 245

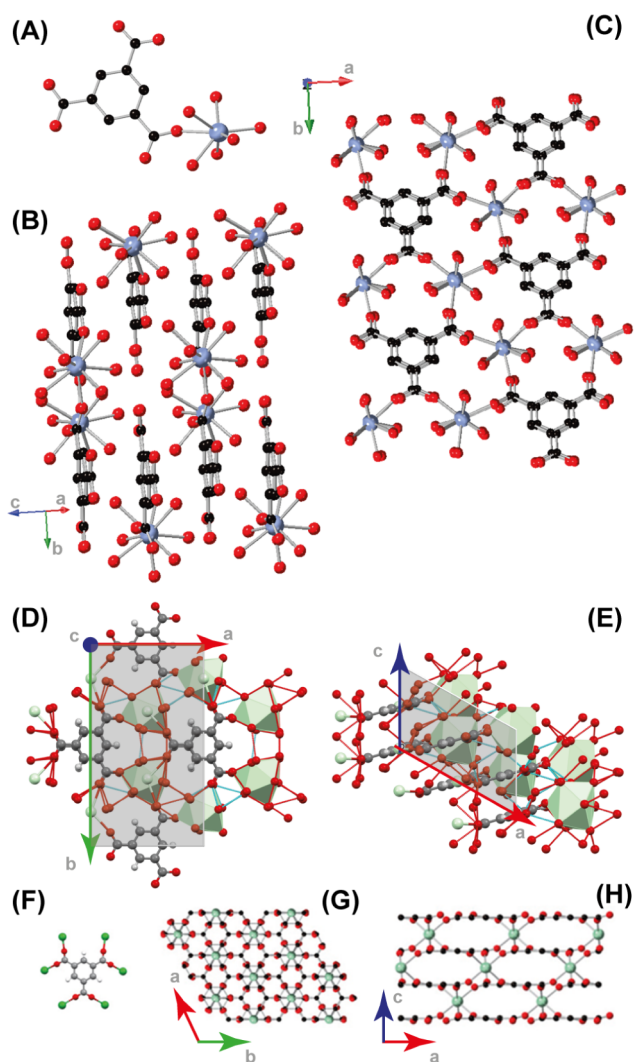


**Figure 1.** View of (A) the asymmetric unit of 1, (B) 1D ribbons running parallel to the *b*-axis, and (C) stacked ribbons in the *ab* plane [001 view]. Sketch of the rich 3D hydrogen-bond framework (dashed red contacts) viewed along the (D) *c*- and (E) *b*-axis. View of (F) one BTC linker coordinating six Yb<sup>III</sup> ions, (G) 3D CP in the *ab* plane, showing Yb<sup>III</sup> ions stacked along the same *c* axis of aromatic BTC ring, (H) 3D CP in the *ac* plane, evidencing Yb<sup>III</sup> and BTC lying in different planes. The black, red, and pastel (green) spheres represent the C, O, and Nd (Yb) atoms, respectively, while H atoms are omitted for clarity.



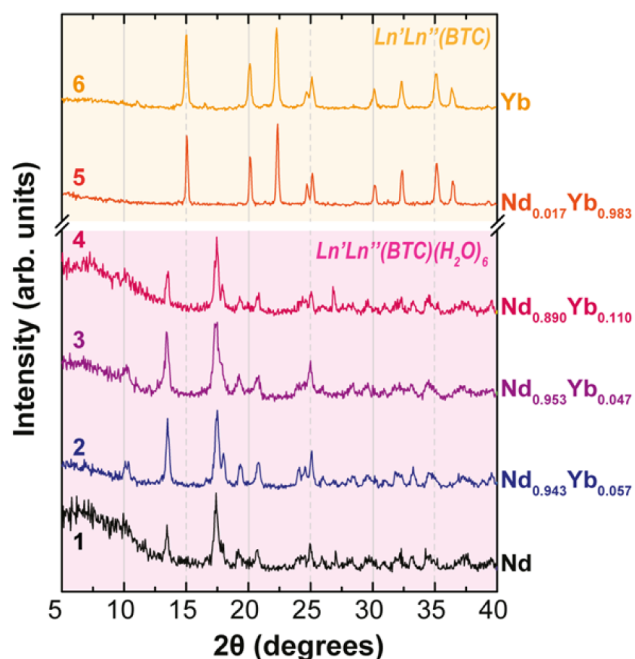


Figure 2. Powder X-ray diffraction patterns in the 5–40°  $2\theta$  range.

246 10000 for MOFs). Thus, as anticipated, our materials are  
247 nonporous and, accordingly, cannot be classified as MOFs.<sup>53,54</sup>

248 FT-IR spectra of 1–6 CPs show the typical bands assigned  
249 to the symmetric and antisymmetric stretching vibrations of  
250 carboxylic groups of trimesic acid<sup>55</sup> (near 1700  $\text{cm}^{-1}$  and in  
251 the 1650–1550 and 1450–1350  $\text{cm}^{-1}$  ranges, Figure S4).  
252 Since carboxylates can coordinate in different modes  
253 (monodentate, bidentate, bridging, etc.), the frequency  
254 separation between the carboxylate antisymmetric and  
255 symmetric stretching vibrations ( $\Delta\nu_{\text{a-s}}$ ) can be related to the  
256 different coordination modes.<sup>56</sup> In fact, in 1–6,  $\Delta\nu_{\text{a-s}}$  (falling in  
257 the 170–180  $\text{cm}^{-1}$  range) can be assigned, in agreement with  
258 the aforementioned crystal structures, to the bridging  
259 coordination mode. All 1–6 CPs show Ln–O stretching  
260 vibrational bands in the 600–400  $\text{cm}^{-1}$  region.<sup>57</sup>

261 **Thermogravimetric Analysis.** TGA thermograms of 1 and 6  
262 were measured to study the thermal stability and confirm the  
263 water content of the two representative structures. 1 shows  
264 four weight losses: a first one (below 70 °C) of about 1.5%,  
265 related to residual moisture; a second one of about 20% at 106  
266 °C, and a third one of 4% at 298 °C, consistent with the  
267 elimination of the six water molecules. At higher temperatures,  
268 500–700 °C, probably the three carboxylate groups are lost, as  
269 previously reported for metal-BTC MOFs,<sup>58,59</sup> and a 40%  
270 weight loss is attributed to the decomposition to  $\text{Nd}_2\text{O}_3$   
271 (Figure S5a). The thermogram of 6 confirms the absence of  
272 water in the structure and its thermal stability up to 400 °C. A  
273 6% sharp loss at about 420 °C is due to a small amount of  
274 trimesic acid impurity (see Figure 2, PXRD peak at about 11°).  
275 A further increase in the temperature led to a >40% weight  
276 loss, with the formation of  $\text{Yb}_2\text{O}_3$  above 500 °C (Figure S5b).  
277 Variable temperature X-ray diffraction analyses, described in  
278 detail in Text S2, enabled structural variations and quantitative  
279 measurement of anisotropic thermal expansion effects,  
280 demonstrating, *inter alia*, the stability range of these materials  
281 when heated in air.

282 **Photophysical Properties.** To further probe the presence of  
283 both metals in the same CPs, diffuse reflectance (DR) spectra

were performed in the 200–2000 nm range. DR spectra of 1– 284  
6 show absorption bands at ~1970, 1660, and 290 nm, due to 285  
the BTC linker. In 1–4 compounds (reported in Figure S7a), 286  
the absorption bands of  $\text{Nd}^{\text{III}}$  ions are observed at 872 nm 287  
( $^4\text{I}_{9/2} \rightarrow ^4\text{F}_{3/2}$ ), 798 nm ( $^4\text{I}_{9/2} \rightarrow ^4\text{F}_{5/2}$ ), 740 nm ( $^4\text{I}_{9/2} \rightarrow$  288  
 $^4\text{F}_{7/2}$ ), 680 nm ( $^4\text{I}_{9/2} \rightarrow ^4\text{F}_{9/2}$ ), 578 nm ( $^4\text{I}_{9/2} \rightarrow ^2\text{G}_{7/2}$ ), 524 289  
nm ( $^4\text{I}_{9/2} \rightarrow ^4\text{G}_{7/2} + ^4\text{G}_{9/2}$ ), 513 nm ( $^4\text{I}_{9/2} \rightarrow ^4\text{G}_{9/2}$ ), and 355 290  
nm ( $^4\text{I}_{9/2} \rightarrow ^4\text{D}_{5/2} + ^4\text{D}_{3/2}$ ). In 2–4, a further band at 980 nm 291  
is observed, confirming the presence of  $\text{Yb}^{\text{III}}$  ( $^2\text{F}_{7/2} \rightarrow ^2\text{F}_{5/2}$ ) in 292  
the CPs.<sup>60–62</sup> Compound 5 shows the absorption bands of 293  
both  $\text{Nd}^{\text{III}}$  and  $\text{Yb}^{\text{III}}$  ions when compared to 6, which exhibits 294  
only the  $\text{Yb}^{\text{III}}$  absorption band, as shown in Figure S7. 295

Figure 3A shows the emission spectra of 1, 4, and 5. 296 f3  
Compounds 1 and 4 show the typical  $\text{Nd}^{\text{III}}$  emission bands 297  
related to the  $^4\text{F}_{3/2} \rightarrow ^4\text{I}_{11/2}$  transition.<sup>46,62</sup> In the case of 4, 298  
 $\text{Yb}^{\text{III}}$  is present and the  $\text{Yb}^{\text{III}}$   $^2\text{F}_{5/2} \rightarrow ^2\text{F}_{7/2}$  emission appears as 299  
a faint band at 980 nm.<sup>46</sup> However, this band is not present in 300  
compound 5 due to (i) the low concentration of  $\text{Nd}^{\text{III}}$  ions 301  
once the excitation is at 580 nm and (ii) the presence of a 302  
center of inversion at the Ln<sup>III</sup> site ( $\text{O}_h$  point group symmetry) 303  
in the  $\text{Nd}_x\text{Yb}_{(1-x)}(\text{BTC})$  structure (Figure S13b). The 304  
presence of a center of inversion does not affect the magnetic 305  
dipole transitions but affects the electric dipole interaction.<sup>63</sup> 306  
Thus, from selection rules on  $J$  quantum number ( $|J - J'| = 0$  307  
or 1), it is expected that the  $\text{Nd}^{\text{III}}$   $^4\text{F}_{3/2} \rightarrow ^4\text{I}_J$  ( $J = 13/2, 11/2,$  308  
 $9/2$ ) emissions present very weak intensities with vibronic and 309  
quadrupole<sup>64</sup> as main interactions. This spectroscopic feature 310  
could also be observed from the poor emission intensity and 311  
emission quantum yield (Table S5) of 5 regarding the second- 312  
order emission peak at 1160 nm (Figure S12) while Figure S10 313  
shows that the second-order peaks are weaker for non- 314  
centrosymmetric CPs. The emission quantum yields for direct 315  
excitation in  $\text{Nd}^{\text{III}}$  (808 nm) and  $\text{Yb}^{\text{III}}$  (980 nm) are  $0.022 \pm$  316  
 $0.002\%$  and  $0.0030 \pm 0.0003\%$  (Table S5). 317

Among the compounds containing mostly  $\text{Nd}^{\text{III}}$  ions (2–4), 318  
4 is the most promising system for ratiometric temperature 319  
measurement because of its higher emission intensity and 320  
emission quantum yield (Table S5), when compared to those 321  
of the other samples. Moreover, it presents a larger variation of 322  
relative intensities with temperature. The temperature-depend- 323  
ent photoluminescence intensity was studied to establish its 324  
potential as a new luminescent thermometer. The thermo- 325  
metric properties of the  $\text{Nd}_x\text{Yb}_{(1-x)}(\text{BTC})$  compounds were 326  
not investigated due to their low emission intensities, as 327  
discussed before. 328

Compound 4 shows two bands at 980 and 1058 nm (Figure 329  
3A), attributed to the  $\text{Yb}^{\text{III}}$   $^2\text{F}_{5/2} \rightarrow ^2\text{F}_{7/2}$  and  $\text{Nd}^{\text{III}}$   $^4\text{F}_{3/2} \rightarrow$  330  
 $^4\text{I}_{11/2}$  transitions, respectively. The relative intensity of  $\text{Yb}^{\text{III}}$  331  
increases when decreasing the temperature and slight changes 332  
in the relative intensities between  $\text{Yb}^{\text{III}}$  and  $\text{Nd}^{\text{III}}$  emission 333  
bands at 1000 and 1057 nm, respectively, are observed at 334  
different temperatures (Figure 4B). 335 f4

Additionally, at 300 K, the  $\text{Yb}^{\text{III}}$  and  $\text{Nd}^{\text{III}}$  emission lifetimes 336  
in 4 are  $\tau_{\text{Yb}}(4) = 7.0 \pm 0.3 \mu\text{s}$  and  $\tau_{\text{Nd}}(4) = 51 \pm 1 \text{ ns}$ , 337  
respectively, as reported in Figure 3B,C. The short lifetimes of 338  
 $\text{Nd}^{\text{III}}$   $^4\text{F}_{3/2}$  can be attributed to a strong electron–phonon 339  
interaction<sup>65–67</sup> and, once it depends on the material, it was 340  
also detected in 1 ( $\tau_{\text{Nd}}(1) = 50 \pm 1 \text{ ns}$ , Figure S11). 341

This reflects a misapprehension of the usage of eqs 1 and 2 342  
for estimations of experimental energy transfer and efficiencies. 343  
Furthermore, with the help of theoretical  $\text{Nd}^{\text{III}} \rightarrow \text{Yb}^{\text{III}}$  energy 344  
transfer calculations, we will show in the next section that eqs 345

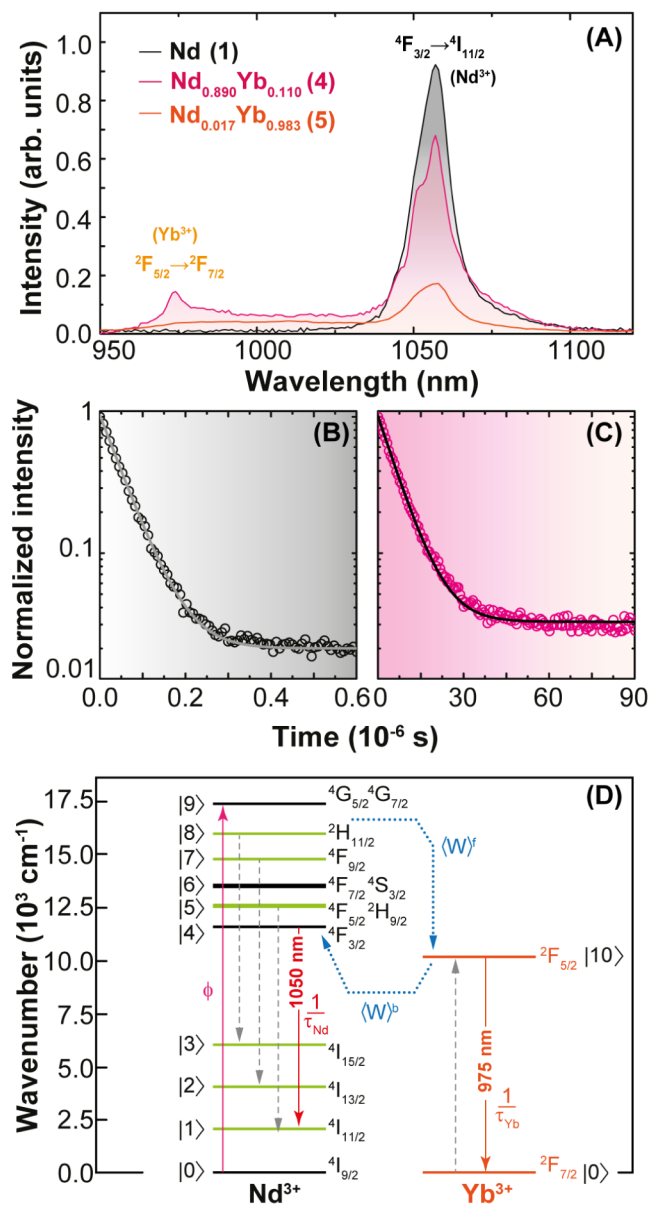


**Figure 3.** (A) Room temperature emission spectra of **1**, **4**, and **5** upon 580 nm excitation. Temporal dynamics decay traces of **4** upon 801 nm laser excitation monitoring the Nd<sup>III</sup> and Yb<sup>III</sup> emitting levels at (B) 1058 nm (<sup>4</sup>F<sub>3/2</sub>) and (C) 975 nm (<sup>2</sup>F<sub>5/2</sub>). (D) Jablonski-type energy level diagram depicting the Nd–Yb energy transfer process.  $\phi$  is the pumping rate  $^4I_{9/2} \rightarrow [^4G_{5/2}, ^4G_{7/2}]$  when Nd<sup>III</sup> is excited at 580 nm.  $\tau_{Nd}$  and  $\tau_{Yb}$  are the decay lifetimes of the Nd<sup>III</sup> and Yb<sup>III</sup> emitting levels, respectively.  $\langle W \rangle^f$  and  $\langle W \rangle^b$  are the average Nd<sup>III</sup>-to-Yb<sup>III</sup> forward and backward energy transfer rates, respectively. The dashed straight lines on the Nd<sup>III</sup> side (involving the green levels) are the main energy transfer pathways that have more contributions to  $\langle W \rangle$ . These rates consider the amount of each ion and their distribution in the compound.

346 and **12** using the Nd<sup>III</sup> <sup>4</sup>F<sub>3/2</sub> decay lifetimes are no longer valid  
 347 because the energy transfer pathways involving this level  
 348 represent less than 1% of the whole Nd<sup>III</sup> → Yb<sup>III</sup> energy  
 349 transfer process. Consequently, this aspect enables the  
 350 extraction of Yb<sup>III</sup> <sup>2</sup>F<sub>5/2</sub> → <sup>2</sup>F<sub>7/2</sub> integrated intensity ( $I_{Yb}$ ) by  
 351 simple subtraction of the whole integrated area from 950 to  
 352 1100 nm by Nd<sup>III</sup> <sup>4</sup>F<sub>3/2</sub> → <sup>4</sup>I<sub>11/2</sub> in **1** (Figure 4A), as it will be  
 353 presented in the Luminescence thermometry subsection.

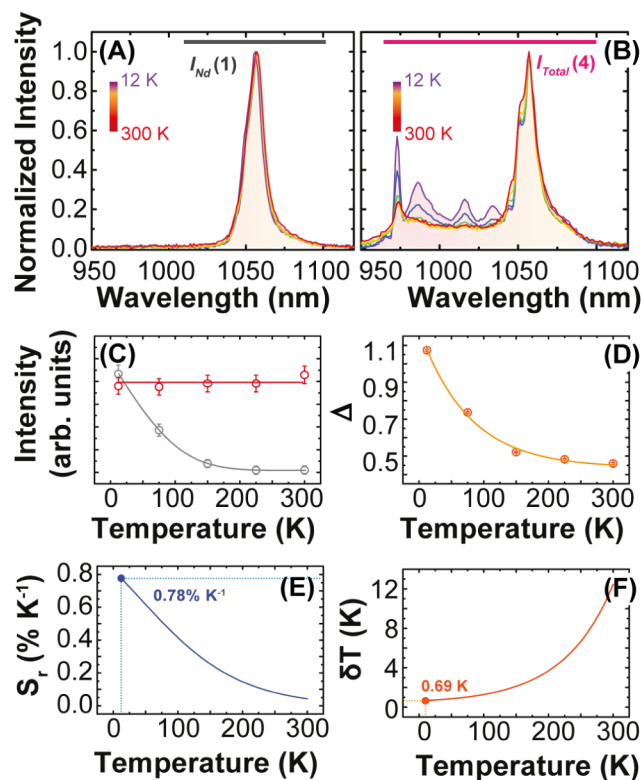


**Figure 4.** Emission spectra of (A) **1** and (B) **4** recorded in the 12–300 K range under 580 nm excitation. (C) Temperature dependence of  $I_{Yb}$  (in gray) and  $I_{Nd}$  (in red) integrate intensities. (D) Thermometric parameter  $\Delta = I_{Yb}/I_{Nd}$ . (E) Relative sensitivity  $S_r$  and (F) temperature uncertainty  $\delta T$  for **4**.

**Nd<sup>III</sup>-to-Yb<sup>III</sup> Energy Transfer.** The energy transfer (ET) 354  
 rates between a pair of lanthanide ions were calculated 355  
 considering the Kushida–Malta model,<sup>68,69</sup> which considers 356  
 dipole–dipole ( $W_{d-d}$ ), dipole–quadrupole ( $W_{d-q}$ ), quadrupole– 357  
 quadrupole ( $W_{q-q}$ ), exchange ( $W_{ex}$ ), and magnetic 358  
 dipole–magnetic dipole ( $W_{md-md}$ ) mechanisms, as defined by 359  
 eqs S9–S13), respectively.<sup>39,69</sup> The ET pathways were selected 360  
 according to energy mismatch conditions (donor–acceptor 361  
 energy difference,  $\delta$ , in Table S7) and selection rules on the  $J$  362  
 quantum numbers: 363

- Electric dipole interactions follows the traditional Judd– 364  
 Ofelt<sup>70,71</sup> selection rule:  $|J - J'| \leq \lambda \leq J + J'$  (with  $\lambda =$  365  
 2, 4, and 6); 366
- Electric quadrupole interactions:  $|J - J'| \leq 2$ ; 367
- Magnetic dipole interaction:  $|J - J'| = 0$  or 1 (except the 368  
 case of  $J = J' = 0$ ). 369

There are no defined selection rules for the isotropic 370  
 contribution of the exchange mechanism ( $W_{ex}$ ).<sup>69</sup> 371

For an illustration of how the above selection rules work, 372  
 consider pathway 17 in Tables S8–S11, which involves the 373  
 donor transition <sup>4</sup>F<sub>3/2</sub> → <sup>4</sup>I<sub>11/2</sub> (Nd<sup>III</sup>) transferring energy to 374  
 the acceptor transition <sup>2</sup>F<sub>7/2</sub> → <sup>2</sup>F<sub>5/2</sub> (Yb<sup>III</sup>) (Figure 3D). We 375  
 can expect contributions from the  $W_{d-d}$  mechanism because 376  
 both transitions obey the electric dipole selection rule. The 377  
 squared reduced matrix elements  $\langle ^4I_{11/2} || U^{(\lambda)} || ^4F_{3/2} \rangle^2$  are 378  
 nonzero for  $\lambda = 4$  and 6 (see Table S12) since  $4 \leq \lambda \leq 7$  379  
 (for this Nd<sup>III</sup> transition). Similarly, the Yb<sup>III</sup> transition has 380  
 contributions from all  $\langle ^2F_{5/2} || U^{(\lambda)} || ^2F_{7/2} \rangle^2$  because  $1 \leq \lambda \leq 6$ . 381

382 However, the dipole–quadrupole mechanism for the same  
383 pathway only has the contribution of the first term of eq S10  
384 (donor by electric dipole and acceptor by electric quadrupole)  
385 because  $\langle {}^4I_{11/2} || U^{(2)} || {}^4F_{3/2} \rangle^2 = 0$ , annulling the second term  
386 (donor by quadrupole and acceptor by dipole). Similarly, the  
387 ET rate for the quadrupole–quadrupole mechanism ( $W_{q-q}$ , eq  
388 S11) for this pathway is zero since the selection rule on  $J$  for  
389 the donor transition is not fulfilled ( $|11/2 - 3/2| > 2$  does  
390 not satisfy the condition  $|J - J'| \leq 2$ ).

391 The sum of all mechanisms for a given pathway  $p$  (e.g.,  $\text{Nd}^{\text{III}}$   
392 [ ${}^4F_{3/2} \rightarrow {}^4I_{9/2}$ ]  $\Rightarrow$   $\text{Yb}^{\text{III}}$  [ ${}^2F_{7/2} \rightarrow {}^2F_{5/2}$ ]) is expressed as  $\omega(p)$ ,  
393 while the sum of all pathways is defined as the total pairwise  
394 energy transfer rate  $W = \sum \omega$ . Tables S8–S11 show the  
395 pairwise energy transfer rates for the Nd–Yb distances of 5.85,  
396 7.03, 7.26, and 8.66 Å, respectively. In these tables, each iT  
397 pathway “ $p$ ” (i.e., a calculated ET rate consisting of one donor  
398 transition and one acceptor transition) is labeled as  $\omega_i^l(p)$ ,  
399 where the superscript letter “ $l$ ” represents the energy transfer  
400 direction ( $f$  and  $b$  stand for forward and backward) and the  
401 subscript “ $i$ ” represents the  $\text{Nd}^{\text{III}}$ – $\text{Yb}^{\text{III}}$  distances order from  
402 the crystallographic structure ( $i = 1, 2, 3$ , and 4 for respective of  
403  $R(i) = 5.85, 7.03, 7.26$ , and 8.66 Å).  $W_i^f$  is the sum of all 64 ET  
404 pathways. Thus, as an example,  $W_i^f$  is the forward  $\text{Nd}^{\text{III}} \rightarrow \text{Yb}^{\text{III}}$   
405 energy transfer when  $\text{Nd}^{\text{III}}$ – $\text{Yb}^{\text{III}}$  distance is 5.85 Å.

406 Concerning the ET pathways with contributions from the  
407  $\text{Nd}^{\text{III}}$   ${}^4F_{3/2}$  level (i.e.,  ${}^4F_{3/2} \rightarrow {}^4I_j$ , pathways  $p = 1, 17, 33$ , and  
408 49 in Tables S8–S11), the sum of them together for each Nd–  
409 Yb distance are 410, 95, 75, and 19  $\text{s}^{-1}$  which represents 0.7%,  
410 1.0%, 1.0%, and 1.4% of the total ET rate, respectively. This  
411 result implies that transitions from  $\text{Nd}^{\text{III}}$   ${}^4F_{3/2}$  level are not  
412 important for the case of the  $\text{Nd}^{\text{III}}$ – $\text{Yb}^{\text{III}}$  ET process and, as a  
413 result, the usage of eqs 1 and 2) considering the lifetimes of  
414 this level is not enough to estimate the experimental rate and  
415 efficiency. On the other hand, the most relevant ET pathways  
416 are from [ ${}^2H_{11/2} \rightarrow {}^4I_{15/2}$ ], [ ${}^4F_{9/2} \rightarrow {}^4I_{13/2}$ ], and [ ${}^2H_{9/2}/{}^4F_{5/2}$   
417  $\rightarrow {}^4I_{11/2}$ ] transitions (see pathways 55, 38, and 18/19 in Tables  
418 S8–S11), representing respectively around 85%, 7%, and 7% of  
419 the total Nd–Yb ET rate. It is worth mentioning that eqs 1, 2)  
420 are still valid for other lanthanide pairs in which the main  
421 donor level is the emitting one, such as the case of Tb–Eu,  
422 where the  $\text{Tb}^{\text{III}}$   ${}^5D_4$  level has an important contribution to the  
423 energy transfer process.<sup>39,41</sup> The dominant mechanism  
424 governing the energy transfer process is the  $W_{q-q}$ , with  
425 pairwise forward ( $\text{Nd}^{\text{III}}$ -to- $\text{Yb}^{\text{III}}$ ) ET rates for pathway 55  
426 ( $\text{Nd}^{\text{III}}$  [ ${}^2H_{11/2} \rightarrow {}^4I_{15/2}$ ]  $\Rightarrow$   $\text{Yb}^{\text{III}}$  [ ${}^2F_{7/2} \rightarrow {}^2F_{5/2}$ ]) in Tables S8–  
427 S11) of  $1.8 \times 10^5$ ,  $2.8 \times 10^4$ , and  $2.0 \times 10^4 \text{ s}^{-1}$  corresponding  
428 to  $\text{Nd}^{\text{III}}$ – $\text{Yb}^{\text{III}}$  distances of 5.85, 7.03, 7.26 Å, respectively. The  
429  $W_{q-q}$  mechanism is also responsible for the backward ET  
430 ( $\text{Yb}^{\text{III}}$ -to- $\text{Nd}^{\text{III}}$ ) process.

431 Once the pairwise  $\text{Nd}^{\text{III}}$ – $\text{Yb}^{\text{III}}$  ET rates are calculated  
432 (Tables S8–S11), we can simulate a Monte Carlo type  
433 distribution of the coordinates of  $\text{Nd}^{\text{III}}$  and  $\text{Yb}^{\text{III}}$  ions in the  
434 host matrix by a homemade program written in C language (it  
435 can be provided upon request). From the crystallographic data  
436 of **1** ( $\text{Nd}(\text{BTC})(\text{H}_2\text{O})_6$  sample), the unit cell ( $1 \times 1 \times 1$ ) was  
437 expanded to a large one ( $20 \times 20 \times 20$ , Figure S14) with a  
438 volume of  $\approx 10378 \text{ nm}^3$  containing 32000  $\text{Nd}^{\text{III}}$  host sites,  
439 which can be replaced randomly by  $\text{Yb}^{\text{III}}$  until reaching the  
440 dopant amount desired (in %). Consequently, the occurrence  
441 of Nd–Yb pair as a function of distance  $n$  and concentration

1 –  $x$  of  $\text{Yb}^{\text{III}}$  throughout the matrix can be obtained and, 442  
consequently, the average forward  $\langle W \rangle^f$  and backward  $\langle W \rangle^b$  443  
energy transfer rates:<sup>41,72</sup> 444

$$\langle W \rangle^f = \sum_i \langle W \rangle_i^f = (1 - x) \cdot x \left( \sum_i O_i(1 - x) W_i^f \right) \quad (3) \quad 445$$

$$\langle W \rangle^b = \sum_i \langle W \rangle_i^b = (1 - x) \cdot x \left( \sum_i O_i(x) W_i^b \right) \quad (4) \quad 446$$

where, as mentioned before,  $W_i^f$  stands for the forward and  $W_i^b$  447  
for the backward energy transfer for the  $i^{\text{th}}$  Nd–Yb distance 448  
(Tables S8–S11). The acceptor  $\text{Yb}^{\text{III}}$  and the donor/host  $\text{Nd}^{\text{III}}$  449  
stoichiometric fractions are represented by  $1 - x$  and  $x$ , 450  
respectively. The occurrence coefficients  $O_i$  are related to the 451  
formation of a Nd–Yb pair at distance  $R(i)$ , regarding the 452  
acceptor (for forward energy transfer  $\langle W \rangle^f$ ) or donor (for 453  
backward energy transfer  $\langle W \rangle^b$ ) amount obtained from 454  
hundreds of Monte Carlo simulations for each  $\text{Yb}^{\text{III}}$  455  
amount:<sup>41,72</sup> 456

$$O_i(1 - x) = \frac{N(i)}{s \cdot (1 - x)}$$

$$O_i(x) = \frac{N(i)}{s \cdot x} \quad (5) \quad 457$$

where  $N(i)$  is the counting of Nd–Yb pairs at distance  $R(i)$  458  
and  $s$  is the number of host sites in the undoped matrix (equals 459  
32000 host sites in the  $20 \times 20 \times 20$  expanded cell, Figure 460  
S14a). Once the backward energy transfer is related to the 461  
energy coming from the  $\text{Yb}^{\text{III}}$  to the  $\text{Nd}^{\text{III}}$  ions, the ‘acceptor’ in 462  
this case is  $\text{Nd}^{\text{III}}$  and it justifies the use of the coefficients  $O_i(x)$  463  
instead of  $O_i(1 - x)$  to calculate the  $\langle W \rangle^b$ . All values of  $O_i$  464  
obtained from simulations as well as  $\langle W \rangle^f$  and  $\langle W \rangle^b$  are 465  
presented in Table S13. 466

Figure S15a shows the total calculated  $\langle W \rangle^b$  with the 467  
changing of the  $\text{Yb}^{\text{III}}$  and  $\text{Nd}^{\text{III}}$  stoichiometric fractions while 468  
Figure S15b shows only the contribution of the backward  $\text{Yb}^{\text{III}}$  469  
[ ${}^2F_{5/2} \rightarrow {}^2F_{7/2}$ ]  $\Rightarrow$   $\text{Nd}^{\text{III}}$  [ ${}^4I_{15/2} \rightarrow {}^2H_{11/2}$ ] pathway, which is 470  
responsible for the quenching of the  $\text{Yb}^{\text{III}}$  emission when 471  
temperature increases, as observed in Figure 4B. The backward 472  
 $\langle W \rangle^b$  is very sensitive to the temperature changes due to the 473  
contribution of about 89% of pathway 55 ( $\text{Nd}^{\text{III}}$  [ ${}^2H_{11/2} \rightarrow$  474  
 ${}^4I_{15/2}$ ]  $\Rightarrow$   $\text{Yb}^{\text{III}}$  [ ${}^2F_{7/2} \rightarrow {}^2F_{5/2}$ ], Tables S8–S11), which has a 475  
close resonant energy mismatch  $\delta$  (Table S7). Our simulations 476  
varied the  $\text{Yb}^{\text{III}}$  amount as given by the synthesized samples ( $1 - x$  477  
 $= 0.047; 0.057; 0.110$ ; representing, respectively, the (3); 478  
(2); (4); samples) and we also extrapolated until  $1 - x = 0.200$  479  
to see the trend of the ET rates. For values of  $\text{Yb}^{\text{III}}$  doped 480  
above this limit, the  $\text{Nd}_x\text{Yb}_{(1-x)}$ (BTC) structure starts to 481  
appear (Figure S2), and once this phase has a  $\text{Ln}^{\text{III}}$  placed at a 482  
centrosymmetric site (Figure S13b), the emission of the  $\text{Ln}^{\text{III}}$  is 483  
quenched.<sup>64</sup> This is the reason we limited the simulations up 484  
to  $1 - x = 0.200$ . 485

Estimation of the emitting level populations (e.g.,  $\text{Nd}^{\text{III}}$   ${}^4F_{3/2}$  486  
and  $\text{Yb}^{\text{III}}$   ${}^2F_{5/2}$ ) requires an effort to build and solve a set of 487  
coupled ordinary differential equations (ODEs) where the 488  
main rates are included, such as Ln–Ln energy transfer, 489  
radiative rates, and multiphonon relaxations. The transient of 490



one level  $P_k$  is represented by solving an 11-level system of rate equations (eqs S19–S29). There are many numerical methods for solving a set of coupled ordinary differential equations;<sup>73</sup> however, we have been using the Radau method<sup>74</sup> because it provided fast and accurate results that were in excellent agreement with other Ln-based luminescence processes.<sup>75–81</sup>

**Experimental and Theoretical Luminescence Thermometry.** Considering the thermal dependence of this energy transfer from Nd<sup>III</sup> to Yb<sup>III</sup>, such systems can be exploited as ratiometric thermometers. First, emission of **1** was studied at different temperatures, as reported in Figure S10, showing a relatively weak signal at 1058 nm, assigned to the Nd<sup>III</sup>  $^4F_{9/2} \rightarrow ^4I_{11/2}$  transition, upon 580 nm excitation. The intensity of the signal is weak considering the excitation of the second order around 1160 nm as a reference and, in this case, no significant changes were observed when decreasing the temperature.

Figure 4A, B displays the temperature dependence from 12 K up to 300 K of **1** and **5** emission spectra upon 580 nm lamp excitation. For both samples, it can be observed that the Nd<sup>III</sup>  $^2F_{3/2} \rightarrow ^4I_{11/2}$  intensity has little temperature dependence, remaining almost constant ( $I_{Nd}$  in Figure 4C). Thus, the intensity of the Yb<sup>III</sup>  $^2F_{5/2} \rightarrow ^2F_{7/2}$  ( $I_{Yb}$ ) transition in sample **4** can be obtained by the subtraction of the integrated intensity  $I_{Nd}$  (highlighted area in Figure 4A) by the integrated intensity  $I_{Total}$  (highlighted area in Figure 4B). This can be assumed because the Nd<sup>III</sup>  $^2F_{3/2} \rightarrow ^4I_{11/2}$  transition is not predominant in the Nd<sup>III</sup> → Yb<sup>III</sup> ET process, as indicated by theoretical calculations.

The distinct temperature dependence of  $I_{Yb}$  and  $I_{Nd}$  indicates that the intensity ratio  $I_{Yb}/I_{Nd}$  is temperature-sensitive and can be used as the thermometric parameter ( $\Delta$ ) for **4**.<sup>6</sup> Figure 4D shows the temperature evolution of  $\Delta$ . As the temperature increases  $\Delta$  decreases in the 12 to 220 K range, remaining constant at this temperature until 300 K, meaning that **4** is temperature-sensitive in the cryogenic range up to 220 K, and mostly insensitive beyond 220 K. The thermal performance of **4** was evaluated through the relative thermal sensitivity ( $S_r$ ), and the temperature uncertainty ( $\delta T$ ), which are the figures of merit to fully characterize the performance of an optical temperature sensor.<sup>5,6,24</sup>

Figure 4E displays  $S_r$  decreasing with temperature from a maximum value of 0.8%·K<sup>-1</sup> at 12 K, reaching less than 0.1%·K<sup>-1</sup> from 250 K and beyond, suggesting the temperature operative range of **4** as optical sensors ranges from 12 K up to 220 K, with a minimum  $\delta T$  of 0.7 at 12 K (Figure 4F). Despite the scarcity of reports on Nd<sup>III</sup>–Yb<sup>III</sup> systems for luminescence thermometry in the cryogenic temperature range, the  $S_r$  values presented in this study are comparable to those previously reported (Table S4). Likewise, the main advantage of our approach is the possibility to rationalize this thermometric performance in terms of the underneath energy transfer processes, as discussed in the following section.

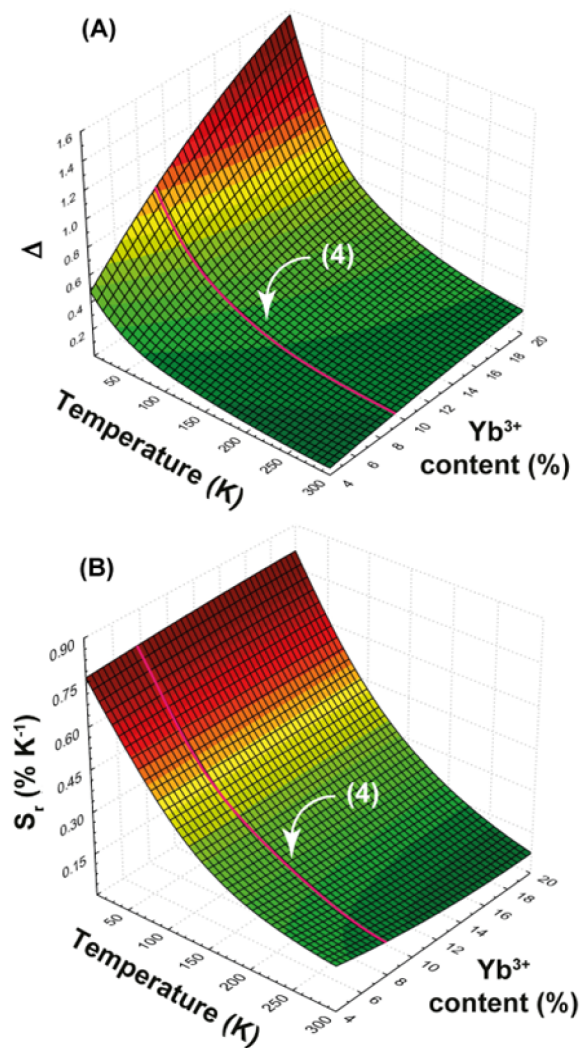
The theoretical thermometric parameters of Nd<sup>III</sup>/Yb<sup>III</sup> mixed CPs were modeled through (i) energy transfer rates between Ln ions,<sup>39,41,69,72</sup> (ii) Judd–Ofelt intensity parameters,<sup>82,83</sup> (iii) Miyakawa–Dexter approach for multiphonon decay rates,<sup>84</sup> and (iv) rate equations modeling.<sup>78,85–88</sup> These building blocks allow us to estimate the relative emission intensity of Yb<sup>III</sup> ( $I_{Yb}$ ) and Nd<sup>III</sup> ( $I_{Nd}$ ), resulting in the theoretical thermometric parameter  $\Delta = I_{Yb}/I_{Nd}$ .

Figure S17a is presented for illustrative purposes and shows a comparison between the experimental and theoretical  $\Delta$  values for sample **4**, assuming  $\tau_{Nd} \approx 50$  ns and  $\tau_{Yb} \approx 7.0$   $\mu$ s (as

measured at room temperature, Figure S11) for all temperatures in our simulations. The discrepancies observed at lower temperatures, indicated by red arrows (Figure S17a), suggest that the lifetimes, particularly  $\tau_{Nd}$ , should be longer. This observation aligns with the temperature dependence of the electron–phonon coupling. To address these discrepancies, Figure S17b demonstrates the mitigation achieved in the simulations by considering longer lifetimes for both  $\tau$  parameters in the low-temperature range below 150 K.

Furthermore, utilizing these theoretical curves, we can deduce that for temperatures below 150 K, the behavior of  $\Delta$  is primarily governed by the Nd<sup>III</sup>–Yb<sup>III</sup> energy transfer, specifically the backward rates involving the Nd<sup>III</sup>  $^2H_{11/2}$  level. On the other hand, at high temperatures, the dominant factor influencing the thermometric parameter is the shortening of  $\tau$ . This unusual shortening of  $\tau_{Nd}$  to the order of 50 ns may potentially be attributed to thermally activated phonons coupling with Nd<sup>III</sup>  $^4F_{3/2}$ , resulting in a fast depopulation of this level.

Figure 5 shows the simulated surfaces of  $\Delta$  and  $S_r$  as a function of Yb<sup>3+</sup> content and temperature. Comparing the highlighted curve in Figure 5A,B (representing the simulation



**Figure 5.** Theoretical (A) thermometric parameter  $\Delta$  and (B) relative thermal sensitivity  $S_r$  as a function of temperature and Yb<sup>III</sup> amount. The magenta lines indicate the simulated curves for **4**.

576 for sample 4) with Figure 4D,E, there is a significant agreement  
577 between the theoretical and experimental data. This finding  
578 supports the earlier discussed point in this article, namely, the  
579 limited involvement of the  $\text{Nd}^{\text{III}}\ ^4\text{F}_{3/2}$  level in the energy  
580 transfer process. Consequently, eqs 1 and 2, which typically  
581 describe energy transfer rates and efficiencies between Ln ions,  
582 do not apply to Nd–Yb interactions unless the excitation  
583 occurs directly in the  $\text{Nd}^{\text{III}}\ ^4\text{F}_{3/2}$  level, not involving the  $\text{Nd}^{\text{III}}$   
584 levels above.

## 585 ■ CONCLUSIONS

586 Two different classes of CPs, formulated, respectively, as  
587  $\text{Nd}_x\text{Yb}_{(1-x)}(\text{BTC})(\text{H}_2\text{O})_6$  ( $x = 1$  (1);  $x = 0.943$  (2);  $x = 0.953$   
588 (3);  $x = 0.890$  (4)) and  $\text{Nd}_x\text{Yb}_{(1-x)}(\text{BTC})$  ( $x = 0.017$  (5),  $x =$   
589 0 (6)), were fully characterized by using a multitechnique  
590 approach to study their structure, morphology, composition,  
591 thermal stability, and optical properties. Particularly, 4 and 5  
592 were selected to perform variable temperature photolumines-  
593 cence studies in the 10–300 K range, which revealed a  
594 decrease of intensity ratio  $\text{Nd}^{\text{III}}/\text{Yb}^{\text{III}}$ -related emission upon  
595 increasing the temperature. This trend is more evident in 4,  
596 which is therefore the most promising system within the entire  
597 series to be employed as a thermometer. The operative range  
598 of the 4 luminescent thermometer ranges from 12 up to 220 K,  
599 with a minimum  $\delta T$  of 0.69 at 12 K. However, rather than  
600 emphasizing the thermometric performance of 4, the objective  
601 of the work is to fully understand the underlying energy  
602 transfer mechanisms and their crucial implications for  
603 optimizing energy transfer-driven ratiometric luminescent  
604 thermometers.

605 Then, theoretical calculations suggested that the Nd–Yb  
606 nonradiative energy transfer comes from a different and  
607 unexpected pathway for both forward ( $\text{Nd}^{\text{III}}\ [^2\text{H}_{11/2}] \rightarrow ^4\text{I}_{15/2}]$   
608  $\rightarrow \text{Yb}^{\text{III}}\ [^2\text{F}_{7/2}] \rightarrow ^2\text{F}_{5/2}]$ ) and backward ( $\text{Yb}^{\text{III}}\ [^2\text{F}_{5/2}] \rightarrow ^2\text{F}_{7/2}]$   
609  $\rightarrow \text{Nd}^{\text{III}}\ [^4\text{I}_{15/2}] \rightarrow ^2\text{H}_{11/2}]$ ) energy transfer. The immediate  
610 outcome of these calculations is that eqs 1 and 2 are not always  
611 valid to estimate the energy transfer rates and efficiency for  
612 Nd–Yb-based materials. Furthermore, the temperature  
613 dependency of  $\text{Nd}_x\text{Yb}_{(1-x)}(\text{BTC})(\text{H}_2\text{O})_6$  CPs is strongly  
614 influenced by the backward pathway and this corroborates  
615 with the observed quenching of the  $\text{Yb}^{\text{III}}$  emission when  
616 temperature increases. This is the first time that a complete ET  
617 analysis on the Nd–Yb pair was done where simulations of  
618 Ln'-to-Ln'' ET-driven thermometers were in good agreement  
619 with the experimental data. Remarkably the present joint  
620 experimental/theoretical work has the potential to pave the  
621 way to a rationalization of NIR luminescent thermometers  
622 based on Nd–Yb energy transfer.

## 623 ■ EXPERIMENTAL SECTION

624 **Materials.** Lanthanide nitrates and the 1,3,5-benzenetricarboxylic  
625 acid were purchased from Alfa Aesar and Sigma-Aldrich, and then  
626 used without further purification.

627 **Synthesis.** All  $\text{Nd}_x\text{Yb}_{(1-x)}\text{BTC}(\text{H}_2\text{O})_6$  ( $x = 1$  (1);  $x = 0.943$  (2);  $x$   
628  $= 0.953$  (3);  $x = 0.890$  (4)) and  $\text{Nd}_x\text{Yb}_{(1-x)}\text{BTC}$  ( $x = 0.017$  (5),  $x = 0$   
629 (6)) compounds were prepared according to the previously reported  
630 method<sup>48</sup> as follows: 0.5 mmol of  $\text{Ln}^{\text{III}}$  precursor ( $\text{Nd}(\text{NO}_3)_3 \cdot 6\text{H}_2\text{O}$   
631 for 1 and  $\text{Yb}(\text{NO}_3)_3 \cdot 6\text{H}_2\text{O}$  for 6) was mixed with 0.5 mmol of  
632  $\text{H}_3\text{BTC}$  (1,3,5-benzenetricarboxylic acid) and ground in an agate  
633 mortar for 5 min. Then the mixture was transferred into a 25 mL  
634 boron-silicate vial and heated at 130 °C for 24 h. After cooling to  
635 room temperature, the powder was collected and washed with  
636 distilled water and ethanol two times each and then dried at 60 °C for  
637 3 h. For the synthesis of compounds 2–5, the procedure was the same

but the two  $\text{Ln}^{\text{III}}$  nitrates were mixed in different Nd/Yb 638  
stoichiometric ratios: from 95/5 to 80/20 (2–4) and 5/95 (5). 639  
The syntheses here proposed typically provide the final products in 640  
100–300 mg amounts and are highly reproducible. Therefore, using 641  
batches from parallel preparations can easily lead to the accumulation 642  
of gram-sized samples. The conventional pathway to obtain these 643  
materials involves the use of hydrothermal methods. Although 644  
ancillary to this work, these recipes are here presented: compounds 645  
1 and 6 were synthesized via a hydrothermal approach. A mixture of 646  
 $\text{Ln}(\text{NO}_3)_3 \cdot 6(\text{H}_2\text{O})$  ( $\text{Ln}^{\text{III}} = \text{Nd, Yb}$ , (0.05 mmol),  $\text{H}_3\text{BTC}$  (0.15 647  
mmol),  $\text{NaOH}$  (1.5 mmol), and water (25 mL) was heated at 120 °C 648  
for 24 h in a 50 mL Teflon-lined stainless-steel autoclave reactor. After 649  
cooling, a white powder, suitable for further characterizations, was 650  
obtained. 651

**ICP-MS.** Inductively coupled plasma spectroscopy (ICP) was 652  
performed on an Agilent Technologies ICP-MS 7900 spectrometer. 653  
The samples were prepared by using microwave digestion in an acid 654  
solution (5 mg of sample in 500  $\mu\text{L}$  of concentrated  $\text{HNO}_3$ ) followed 655  
by dilution with water (5 mL final volume). 656

**Infrared Spectroscopy.** FT-IR spectra were collected using a 657  
Bruker Equinox 55 spectrometer, with the samples prepared as KBr 658  
pellets (Figure S4). 659

**Brunauer–Emmett–Teller (BET) Analyses.** The textural 660  
properties were studied by nitrogen adsorption–desorption isotherms 661  
at  $-196$  °C, measured on a Micromeritics ASAP 2020 system. The 662  
samples were preheated under vacuum at 50 °C (heating rate, 1 °C· 663  
 $\text{min}^{-1}$ ) for 12 h. BET SSA values found: 37  $\text{m}^2 \cdot \text{g}^{-1}$  for  $\text{Nd}(\text{BTC})$ - 664  
 $(\text{H}_2\text{O})_6$  and 20  $\text{m}^2 \cdot \text{g}^{-1}$  for  $\text{Yb}(\text{BTC})$  (Text S3). 665

**EDX Microanalysis.** SEM images and EDX Microanalysis were 666  
performed both on a Hitachi S-4800 and ESEM:FEI Quanta 200 field 667  
emission scanning electron microscopes (Tables S2–S3 and Figure 668  
S6). 669

**Thermogravimetric Analysis.** Thermogravimetric analysis was 670  
performed in alumina crucibles with the instrument STA-6000 under 671  
nitrogen flux (40 mL/min) in the 25–800 °C temperature range at 10 672  
°C/min. 673

**Powder X-Ray Diffraction.** PXRD patterns for fingerprinting 674  
purposes were collected by using a  $\theta$ – $\theta$  Bragg–Brentano focalizing 675  
geometry Seifert X 3000 diffraction system equipped with a Cu  $K\alpha$  676  
source ( $\lambda = 1.5418$  Å), a graphite monochromator on the diffracted 677  
beam, and a scintillation counter. Step size 0.05°, acquisition time 2 s/ 678  
step. Structural PXRD studies require a more careful sample 679  
preparation, data collection strategy, and several computational 680  
steps (indexing, structure solution, and Rietveld refinement) 681  
collectively presented in the SI file. CSD Codes: 2212923–2212924. 682

**Dynamic Light Scattering (DLS).** The suspensions of Nd/Yb 683  
CPs in water/DMSO were prepared by suspending 2 mg of 684  
microcrystalline powder in 2 mL of solvent and ultrasonating it 685  
for 15 min. Then they were diluted (200  $\mu\text{L}$  of suspension and 800  $\mu\text{L}$  686  
of solvent) to allow DLS performed with the Malvern ZETASIZER 687  
NANO instrument. 688

**Photophysical Measurements.** Continuous-wave diffuse reflectance 689  
of crystals of coordination compounds was performed with a 690  
dual-beam spectrophotometer equipped with an integrating sphere 691  
accessory (Agilent Cary 5000 UV–vis–NIR). Emission and excitation 692  
spectra were recorded on a modular double grating excitation 693  
spectrofluorimeter with a TRIAX 320 emission monochromator 694  
(Fluorolog-3, Horiba Scientific) coupled to an NIR H9170 695  
Hamamatsu photomultiplier, using the front face acquisition mode. 696  
The excitation source was a 450 W xenon arc lamp. The excitation 697  
spectra were corrected for the spectral distribution of the lamp 698  
intensity by using a photodiode reference detector. Time-resolved 699  
measurements were carried out with pulsed Xe–Hg lamp excitation in 700  
front face acquisition mode. The low-temperature measurements (12 701  
K) were performed using a helium-closed cycle cryostat with a 702  
vacuum system measuring ca.  $5 \times 10^{-6}$  mbar and a Lakeshore 330 703  
autotuning temperature controller with a resistance heater. 704



## 705 ■ THEORETICAL SECTION

706 **Nd–Yb Energy Transfer.** The pairwise energy transfer  
707 rates for Nd–Yb are calculated from eqs S9–S13 according to  
708 the procedures described in refs.<sup>39,69</sup> (see [Supporting](#)  
709 [Information](#) for more details). The distribution of Nd<sup>III</sup> and  
710 Yb<sup>III</sup> and the average energy transfer rates (from the pairwise  
711 Nd–Yb rates) were calculated using the method described in  
712 ref.<sup>41</sup>.

713 **Multiphonon Decay Rates.** The nonradiative decay rates  
714 between adjacent levels of Nd<sup>III</sup> ion were calculated using the  
715 Miyakawa–Dexter model as described in [Supporting Informa-](#)  
716 [tion](#) and refs.<sup>84</sup>.

717 **Rate Equations.** A general differential rate equation has  
718 the general form:<sup>78,85–88</sup>

$$\frac{d}{dt}P_k(t) = \sum_{j \neq k} W_{j \rightarrow k} P_j(t) - \sum_{j \neq k} W_{k \rightarrow j} P_k(t) \quad (6)$$

720 where the summations run the levels of the system.  $P_k$  and  $P_j$   
721 are the populations of the levels  $|k\rangle$  and  $|j\rangle$ ,  $W_{j \rightarrow k}$  and  $W_{k \rightarrow j}$  are  
722 rates between these states (Nd<sup>III</sup>–Yb<sup>III</sup> energy transfer or decay  
723 processes). The first summation represents all rates that enter  
724 in  $|k\rangle$ , while the second represents those that depart from  $|k\rangle$ .  
725 The complete set of the rate equation model is given by the  
726 coupled equations (eqs S19–S29).

727 **Intensity Parameters and Radiative Rates.** The Judd–  
728 Ofelt intensity parameters were calculated using the Simple  
729 Overlap Model (SOM)<sup>83</sup> for the odd component of the ligand  
730 field and the Bond Overlap Model (BOM)<sup>82</sup> for the  
731 polarizability-dependent term. The radiative rates are calcu-  
732 lated using eqs S31–S33 (see [Supporting Information](#) for  
733 further details).

734 **Thermometric Parameter and Relative Thermal**  
735 **Sensitivity.** The experimental  $\Delta$  was defined as  $\Delta = I_{\text{Yb}}/I_{\text{Nd}}$   
736 , where  $I_{\text{Yb}}$  and  $I_{\text{Nd}}$  are the integrated intensity of the  ${}^2\text{F}_{5/2} \rightarrow$   
737  ${}^2\text{F}_{7/2}$  and  ${}^4\text{F}_{3/2} \rightarrow {}^4\text{I}_{11/2}$  emissions, respectively. Thus, the  
738 theoretical  $\Delta$  is given by

$$\Delta = \frac{I_{\text{Yb}}}{I_{\text{Nd}}} = \frac{A_{\text{rad}}(\text{Yb}) \cdot P_{10}}{A_{\text{rad}}(\text{Nd}) \cdot P_4} \quad (7)$$

740 where  $A_{\text{rad}}$  is the radiative component of the  ${}^2\text{F}_{5/2} \rightarrow {}^2\text{F}_{7/2}$   
741 and  ${}^4\text{F}_{3/2} \rightarrow {}^4\text{I}_{11/2}$  transitions.  $P_{10}$  and  $P_4$  represent the  
742 calculated populations of the Yb<sup>III</sup>  ${}^2\text{F}_{5/2}$  and Nd<sup>III</sup>  ${}^4\text{F}_{3/2}$   
743 emitting levels in the steady-state regime, respectively. The  
744 thermal sensitivity is given by

$$S_r = \frac{1}{\Delta} \left| \frac{\partial \Delta}{\partial T} \right| \quad (8)$$

746 as defined for the experimental one.

## 747 ■ ASSOCIATED CONTENT

### 748 **SI** Supporting Information

749 The Supporting Information is available free of charge at  
750 <https://pubs.acs.org/doi/10.1021/acs.chemmater.4c00362>

751 Powder X-ray diffraction; FT-IR spectra; thermogravi-  
752 metric analysis; EDX microanalysis, ICP-MS data, and  
753 SEM images; photophysical characterization; materials  
754 stability by DLS and PXRD measurements; performance  
755 of Nd<sup>III</sup>/Yb<sup>III</sup>-based luminescent thermometers; photo-  
756 luminescent properties; theoretical modeling methodol-  
757 ogy; supplementary text 1: an estimate of specific

surface areas; supplementary text 2: thermal stability in  
air; supplementary text 3: textural properties(PDF) 758  
crystallographic data of 1 (Nd(BTC)(H<sub>2</sub>O)<sub>6</sub>)(CIF) 759  
crystallographic data of Nd<sub>x</sub>Yb<sub>(1-x)</sub>(BTC)(H<sub>2</sub>O)<sub>6</sub> (CIF) 760  
761

## 762 ■ AUTHOR INFORMATION

### 763 Corresponding Authors

764 **Albano N. Carneiro Neto** – *Phantom-g, Department of* 764  
*Physics, CICECO-Aveiro Institute of Materials, University of* 765  
*Aveiro, Aveiro 3810-193, Portugal;* [orcid.org/0000-0003-](https://orcid.org/0000-0003-2432-0992) 766  
[2432-0992](https://orcid.org/0000-0003-2432-0992); Email: [albanoneto@ua.pt](mailto:albanoneto@ua.pt) 767

768 **Luís D. Carlos** – *Phantom-g, Department of Physics,* 768  
*CICECO-Aveiro Institute of Materials, University of Aveiro,* 769  
*Aveiro 3810-193, Portugal;* [orcid.org/0000-0003-4747-](https://orcid.org/0000-0003-4747-6535) 770  
[6535](https://orcid.org/0000-0003-4747-6535); Email: [lcarlos@ua.pt](mailto:lcarlos@ua.pt) 771

772 **Maria Laura Mercuri** – *Dipartimento di Scienze Chimiche e* 772  
*Geologiche, Università degli Studi di Cagliari, Monserrato I-* 773  
*09042, Italy; INSTM, Firenze 50121, Italy;* [orcid.org/](https://orcid.org/0000-0002-4816-427X) 774  
[0000-0002-4816-427X](https://orcid.org/0000-0002-4816-427X); Email: [mercuri@unica.it](mailto:mercuri@unica.it) 775

### 776 Authors

777 **Mariangela Oggianu** – *Dipartimento di Scienze Chimiche e* 777  
*Geologiche, Università degli Studi di Cagliari, Monserrato I-* 778  
*09042, Italy; INSTM, Firenze 50121, Italy* 779

780 **Valentina Mameli** – *Dipartimento di Scienze Chimiche e* 780  
*Geologiche, Università degli Studi di Cagliari, Monserrato I-* 781  
*09042, Italy; INSTM, Firenze 50121, Italy* 782

783 **Miguel A. Hernández-Rodríguez** – *Phantom-g, Department* 783  
*of Physics, CICECO-Aveiro Institute of Materials, University* 784  
*of Aveiro, Aveiro 3810-193, Portugal* 785

786 **Noemi Monni** – *Dipartimento di Scienze Chimiche e* 786  
*Geologiche, Università degli Studi di Cagliari, Monserrato I-* 787  
*09042, Italy; INSTM, Firenze 50121, Italy* 788

789 **Manuel Souto** – *Department of Chemistry, CICECO-Aveiro* 789  
*Institute of Materials, University of Aveiro, Aveiro 3810-193,* 790  
*Portugal;* [orcid.org/0000-0003-3491-6984](https://orcid.org/0000-0003-3491-6984) 791

792 **Carlos D.S. Brites** – *Phantom-g, Department of Physics,* 792  
*CICECO-Aveiro Institute of Materials, University of Aveiro,* 793  
*Aveiro 3810-193, Portugal;* [orcid.org/0000-0001-9636-](https://orcid.org/0000-0001-9636-2628) 794  
[2628](https://orcid.org/0000-0001-9636-2628) 795

796 **Carla Cannas** – *Dipartimento di Scienze Chimiche e* 796  
*Geologiche, Università degli Studi di Cagliari, Monserrato I-* 797  
*09042, Italy; INSTM, Firenze 50121, Italy;* [orcid.org/](https://orcid.org/0000-0003-2908-7739) 798  
[0000-0003-2908-7739](https://orcid.org/0000-0003-2908-7739) 799

800 **Fabio Manna** – *Dipartimento di Scienze Chimiche e* 800  
*Geologiche, Università degli Studi di Cagliari, Monserrato I-* 801  
*09042, Italy* 802

803 **Francesco Quochi** – *INSTM, Firenze 50121, Italy;* 803  
*Dipartimento di Fisica, Università degli Studi di Cagliari,* 804  
*Monserrato I-09042, Italy* 805

806 **Enzo Cadoni** – *Dipartimento di Scienze Chimiche e* 806  
*Geologiche, Università degli Studi di Cagliari, Monserrato I-* 807  
*09042, Italy* 808

809 **Norberto Masciocchi** – *Dipartimento di Scienza e Alta* 809  
*Tecnologia & To.Sca.Lab., Università dell'Insubria, Como* 810  
*22100, Italy;* [orcid.org/0000-0001-9921-2350](https://orcid.org/0000-0001-9921-2350) 811

812 Complete contact information is available at:

813 <https://pubs.acs.org/doi/10.1021/acs.chemmater.4c00362>

### 814 Author Contributions

815 <sup>▽</sup>M.O., V.M., and M.A.H.-R. have contributed equally to this  
work. The manuscript was written through the contributions of 816

817 all authors. All authors have approved the final version of the  
818 manuscript.

### 819 Funding

820 Fondazione di Sardegna—Convenzione triennale tra la  
821 Fondazione di Sardegna e gli Atenei Sardi, Regione  
822 Sardegna—L.R. 7/2007 annualità 2020, through Project  
823 ‘Smart supramolecular Materials for Anion sensing and  
824 Water Remediation (SMAWRT),’ CUP: F75F21001260007,  
825 is acknowledged for financial support. FCT/MCTES—The  
826 Shape of Water (PTDC/NAN-PRO/3881/2020) and Logi-  
827 cALL (PTDC/CTM-CTM/0340/2021) financed by Portu-  
828 guese funds.

### 829 Notes

830 The authors declare no competing financial interest.

### 831 ■ ACKNOWLEDGMENTS

832 This work was developed within the scope of the projects  
833 CICECO-Aveiro Institute of Materials, UIDB/50011/2020  
834 (DOI 10.54499/UIDB/50011/2020), UIDP/50011/2020  
835 (DOI 10.54499/UIDP/50011/2020) & LA/P/0006/2020  
836 (DOI 10.54499/LA/P/0006/2020), The Shape of Water  
837 (PTDC/NAN-PRO/3881/2020), and LogicALL (PTDC/  
838 CTM-CTM/0340/2021) financed by national funds through  
839 the FCT/MCTES (PIDDAC). CESA (Centro d’Eccellenza  
840 per la Sostenibilità Ambientale, accordo di programma RAS-  
841 UNICA-IGEA-AUSI, project number E58C16000080003),  
842 MIUR (Ministry of Education, University, Research) and  
843 UNICA-UNISS Consortium PhD Course on Chemical  
844 Sciences and Technologies are also acknowledged for MO  
845 and NM PhD grants. CeSAR (Centro Servizi d’Ateneo per la  
846 Ricerca) core facility of the University of Cagliari is acknowl-  
847 edged for the use of the Scanning Electron Microscopy  
848 Laboratory. Prof. Miguel Clemente-Leon, University of  
849 Valencia, is also acknowledged for ICP-MS data and helpful  
850 discussion. PON AIM (PON Ricerca e Innovazione 2014–  
851 2020 – Azione I.2 – DD n. 407 del 27 febbraio 2018  
852 “Attraction and International Mobility”, Cult-GeoChim project  
853 AIM1890410-3), and CESA project are gratefully acknowl-  
854 edged for financing the fellowships of V. Mameli. CeSAR  
855 (Centro Servizi d’Ateneo per la Ricerca) of the University of  
856 Cagliari, Italy, is also acknowledged for ESEM-EDX measure-  
857 ments performed with of FEI Company Quanta 200 ESEM  
858 equipped with a Thermo Scientific EDX probe.

### 859 ■ ABBREVIATIONS

860 CP	coordination polymer
861 MOF	metal–organic framework
862 H <sub>3</sub> BTC	1,3,5-benzentricarboxylic acid
863 NIR	near-infrared
864 ET	energy transfer
865 PXRD	powder X-ray diffractometry
866 ICP-MS	induced coupled plasm mass spectrometry
867 SEM-EDX	scanning electron microscopy—energy dispersive X-ray
868 TGA	thermal gravimetric analysis
869 FT-IR	Fourier transformed—infrared spectroscopy
870 DR	diffuse Reflectance spectra

### 872 ■ REFERENCES

873 (1) Michalski, L.; Eckersdorf, K.; Kucharski, J.; McGhee, J.  
874 *Temperature Measurement*, 2nd ed.; John Wiley & Sons: West Sussex,  
875 2002.

- (2) Moldover, M. R.; Tew, W. L.; Yoon, H. W. *Advances in* 876  
*Thermometry. Nat. Phys.* **2016**, *12* (1), 7–11. 877
- (3) Dedyulin, S.; Ahmed, Z.; Machin, G. *Emerging Technologies in* 878  
*the Field of Thermometry. Meas. Sci. Technol.* **2022**, *33* (9), 092001. 879
- (4) Bednarkiewicz, A.; Marciniak, L.; Carlos, L. D.; Jaque, D. 880  
*Standardizing Luminescence Nanothermometry for Biomedical* 881  
*Applications. Nanoscale* **2020**, *12* (27), 14405–14421. 882
- (5) Brites, C. D. S.; Lima, P. P.; Silva, N. J. O.; Millán, A.; Amaral, V. 883  
S.; Palacio, F.; Carlos, L. D. *Thermometry at the Nanoscale.* 884  
*Nanoscale* **2012**, *4* (16), 4799. 885
- (6) Brites, C. D. S.; Balabhadra, S.; Carlos, L. D. *Lanthanide-Based* 886  
*Thermometers: At the Cutting-Edge of Luminescence Thermometry.* 887  
*Adv. Opt. Mater.* **2019**, *7* (5), 1801239. 888
- (7) Nexha, A.; Carvajal, J. J.; Pujol, M. C.; Díaz, F.; Aguiló, M. 889  
*Lanthanide Doped Luminescence Nanothermometers in the Bio-* 890  
*logical Windows: Strategies and Applications. Nanoscale* **2021**, *13* 891  
*(17)*, 7913–7987. 892
- (8) Dramićanin, M. D. *Trends in Luminescence Thermometry. J.* 893  
*Appl. Phys.* **2020**, *128* (4), 040902. 894
- (9) Elliott, G. D.; Wang, S.; Fuller, B. J. *Cryoprotectants: A Review* 895  
*of the Actions and Applications of Cryoprotective Solutes That* 896  
*Modulate Cell Recovery from Ultra-Low Temperatures. Cryobiology* 897  
**2017**, *76*, 74–91. 898
- (10) Afonso, J.; Martins, D.; Catarino, I.; Patrício, R.; Rocabay, A.; 899  
Tirolien, T.; Bonfait, G. *Liquid–Gas Cryogenic Energy Storage Units* 900  
*Operating at Constant Temperature. Appl. Therm. Eng.* **2016**, *95*, 901  
178–185. 902
- (11) Potts, C. A.; Bittencourt, V. A. S. V.; Kusminskiy, S. V.; Davis, J. 903  
P. *Magnon-Phonon Quantum Correlation Thermometry. Phys. Rev.* 904  
*Appl.* **2020**, *13* (6), 064001. 905
- (12) Kale, A.; Khanna, N. *A Review on Cryogenic Machining of* 906  
*Super Alloys Used in Aerospace Industry. Procedia Manuf.* **2017**, *7*, 907  
191–197. 908
- (13) Giordano, V.; Fluhr, C.; Dubois, B. *Magnetic Sensitivity of the* 909  
*Microwave Cryogenic Sapphire Oscillator. J. Appl. Phys.* **2020**, *127* 910  
*(18)*, 184101. 911
- (14) Rosso, L.; Tabandeh, S.; Beltramino, G.; Fericola, V. 912  
*Validation of Phosphor Thermometry for Industrial Surface Temper-* 913  
*ature Measurements. Meas. Sci. Technol.* **2020**, *31* (3), 034002. 914
- (15) Quintanilla, M.; Henriksen-Lacey, M.; Renero-Lecuna, C.; Liz- 915  
Marzán, L. M. *Challenges for Optical Nanothermometry in Biological* 916  
*Environments. Chem. Soc. Rev.* **2022**, *51* (11), 4223–4242. 917
- (16) Bao, G.; Wong, K.-L.; Jin, D.; Tanner, P. A. *A Stoichiometric* 918  
*Terbium–Europium Dyad Molecular Thermometer: Energy Transfer* 919  
*Properties. Light: sci. Appl.* **2018**, *7* (1), 96. 920
- (17) Hasegawa, Y.; Kitagawa, Y. *Thermo-Sensitive Luminescence of* 921  
*Lanthanide Complexes, Clusters, Coordination Polymers and Metal–* 922  
*Organic Frameworks with Organic Photosensitizers. J. Mater. Chem. C* 923  
**2019**, *7* (25), 7494–7511. 924
- (18) Gu, Y.; Piñol, R.; Moreno-Loshuertos, R.; Brites, C. D. S.; 925  
Zeler, J.; Martínez, A.; Maurin-Pasturel, G.; Fernández-Silva, P.; 926  
Marco-Brualla, J.; Téllez, P.; et al. *Local Temperature Increments* 927  
*and Induced Cell Death in Intracellular Magnetic Hyperthermia. ACS* 928  
*Nano* **2023**, *17* (7), 6822–6832. 929
- (19) Savchuk, O. A.; Carvajal, J. J.; Massons, J.; Cascales, C.; Aguiló, 930  
M.; Díaz, F. *Novel Low-Cost Compact and Fast Signal Processing* 931  
*Sensor for Ratiometric Luminescent Nanothermometry. Sens.* 932  
*Actuators, A* **2016**, *250*, 87–95. 933
- (20) Cui, Y.; Xu, H.; Yue, Y.; Guo, Z.; Yu, J.; Chen, Z.; Gao, J.; 934  
Yang, Y.; Qian, G.; Chen, B. *A Luminescent Mixed-Lanthanide* 935  
*Metal–Organic Framework Thermometer. J. Am. Chem. Soc.* **2012**, 936  
*134* (9), 3979–3982. 937
- (21) Cadiau, A.; Brites, C. D. S.; Costa, P. M. F. J.; Ferreira, R. A. S.; 938  
Rocha, J.; Carlos, L. D. *Ratiometric Nanothermometer Based on an* 939  
*Emissive Ln<sup>3+</sup>-Organic Framework. ACS Nano* **2013**, *7* (8), 7213– 940  
7218. 941
- (22) Brites, C. D. S.; Lima, P. P.; Silva, N. J. O.; Millán, A.; Amaral, 942  
V. S.; Palacio, F.; Carlos, L. D. *Ratiometric Highly Sensitive* 943  
*Luminescent Nanothermometers Working in the Room Temperature* 944



- 945 Range. Applications to Heat Propagation in Nanofluids. *Nanoscale*  
946 **2013**, *5* (16), 7572.
- 947 (23) Ferdinandus; Suzuki, M.; Vu, C. Q.; Harada, Y.; Sarker, S. R.;  
948 Ishiwata, S.; Kitaguchi, T.; Arai, S. Modulation of Local Cellular  
949 Activities Using a Photothermal Dye-Based Subcellular-Sized Heat  
950 Spot. *ACS Nano* **2022**, *16* (6), 9004–9018.
- 951 (24) Brites, C. D. S.; Millán, A.; Carlos, L. D. Lanthanides in  
952 Luminescent Thermometry. In *Handbook on the Physics and Chemistry*  
953 *of Rare Earths*, Bünzli, J.-C. G.; Pecharsky, V. K., Eds.; Elsevier, 2016;  
954 Vol. 49, pp. 339427. DOI: .
- 955 (25) Jia, M.; Chen, X.; Sun, R.; Wu, D.; Li, X.; Shi, Z.; Chen, G.;  
956 Shan, C. Lanthanide-Based Ratiometric Luminescence Nanother-  
957 mometry. *Nano Res.* **2023**, *16* (2), 2949–2967.
- 958 (26) Bünzli, J.-C. G.; Piguet, C. Taking Advantage of Luminescent  
959 Lanthanide Ions. *Chem. Soc. Rev.* **2005**, *34* (12), 1048.
- 960 (27) Taarit, L.; Alves, F.; Benchohra, A.; Guénée, L.; Golesorkhi, B.;  
961 Rosspeintner, A.; Fürstenberg, A.; Piguet, C. Seeking Brightness in  
962 Molecular Erbium-Based Light Upconversion. *J. Am. Chem. Soc.* **2023**.
- 963 (28) Rocha, J.; Brites, C. D. S.; Carlos, L. D. Lanthanide Organic  
964 Framework Luminescent Thermometers. *Chemistry* **2016**, *22* (42),  
965 14782–14795.
- 966 (29) Cui, Y.; Zhu, F.; Chen, B.; Qian, G. Metal–Organic  
967 Frameworks for Luminescence Thermometry. *Chem. Commun.*  
968 **2015**, *51* (35), 7420–7431.
- 969 (30) Kanzariya, D. B.; Chaudhary, M. Y.; Pal, T. K. Engineering of  
970 Metal–Organic Frameworks (MOFs) for Thermometry. *Dalt. Trans.*  
971 **2023**, *52* (22), 7383–7404.
- 972 (31) Orlova, A. V.; Kozhevnikova, V. Y.; Goloveshkin, A. S.; Lepnev,  
973 L. S.; Utochnikova, V. V. NIR Luminescence Thermometers Based on  
974 Yb–Nd Coordination Compounds for the 83–393 K Temperature  
975 Range. *Dalt. Trans.* **2022**, *51* (14), 5419–5425.
- 976 (32) Xiang, G.; Yang, M.; Liu, Z.; Wang, Y.; Jiang, S.; Zhou, X.; Li,  
977 L.; Ma, L.; Wang, X.; Zhang, J. Near-Infrared-to-Near-Infrared Optical  
978 Thermometer BaY<sub>2</sub>O<sub>4</sub>: Yb<sup>3+</sup>/Nd<sup>3+</sup> Assembled with Photothermal  
979 Conversion Performance. *Inorg. Chem.* **2022**, *61* (13), 5425–5432.
- 980 (33) Gomez, G. E.; Marin, R.; Botas, A. M. P.; Owens, J.; Kitos, A.  
981 A.; Bernini, M. C.; Carlos, L. D.; Soler-Illia, G. J. A. A.; Murugesu, M.  
982 Tunable Energy-Transfer Process in Heterometallic MOF Materials  
983 Based on 2,6-Naphthalenedicarboxylate: Solid-State Lighting and  
984 Near-Infrared Luminescence Thermometry. *Chem. Mater.* **2020**, *32*  
985 (17), 7458–7468.
- 986 (34) Suo, H.; Zhao, X.; Zhang, Z.; Guo, C. Ultra-Sensitive Optical  
987 Nano-Thermometer LaPO<sub>4</sub>: Yb<sup>3+</sup>/Nd<sup>3+</sup> Based on Thermo-Enhanced  
988 NIR-to-NIR Emissions. *Chem. Eng. J.* **2020**, *389*, 124506.
- 989 (35) Gao, G.; Busko, D.; Kauffmann-Weiss, S.; Turshatov, A.;  
990 Howard, I. A.; Richards, B. S. Wide-Range Non-Contact Fluorescence  
991 Intensity Ratio Thermometer Based on Yb<sup>3+</sup>/Nd<sup>3+</sup> Co-Doped La<sub>2</sub>O<sub>3</sub>  
992 Microcrystals Operating from 290 to 1230 K. *J. Mater. Chem. C* **2018**,  
993 *6* (15), 4163–4170.
- 994 (36) Xu, W.; Hu, Y.; Zheng, L.; Zhang, Z.; Cao, W.; Liu, H.; Wu, X.  
995 Enhanced NIR-NIR Luminescence from CaWO<sub>4</sub>: Nd<sup>3+</sup>/Yb<sup>3+</sup>  
996 Phosphors by Li<sup>+</sup> Codoping for Thermometry and Optical Heating.  
997 *J. Lumin.* **2019**, *208*, 415–423.
- 998 (37) Chen, H.; Bai, G.; Yang, Q.; Hua, Y.; Xu, S.; Chen, L. Non-  
999 Contact Fluorescence Intensity Ratio Optical Thermometer Based on  
1000 Yb<sup>3+</sup>/Nd<sup>3+</sup> Codoped Bi<sub>4</sub>Ti<sub>3</sub>O<sub>12</sub> Microcrystals. *J. Lumin.* **2020**, *221*,  
1001 117095.
- 1002 (38) Xu, W.; Qi, H.; Zheng, L.; Zhang, Z.; Cao, W. Multifunctional  
1003 Nanoparticles Based on the Nd<sup>3+</sup>/Yb<sup>3+</sup> Codoped NaYF<sub>4</sub>. *Opt. Lett.*  
1004 **2015**, *40* (23), 5678.
- 1005 (39) Carneiro Neto, A. N.; Moura, R. T.; Shyichuk, A.; Paterlini, V.;  
1006 Piccinelli, F.; Bettinelli, M.; Malta, O. L. Theoretical and Experimental  
1007 Investigation of the Tb<sup>3+</sup> → Eu<sup>3+</sup> Energy Transfer Mechanisms in  
1008 Cubic A<sub>3</sub>Tb<sub>0.90</sub>Eu<sub>0.10</sub>(PO<sub>4</sub>)<sub>3</sub> (A = Sr, Ba) Materials. *J. Phys. Chem. C*  
1009 **2020**, *124* (18), 10105–10116.
- 1010 (40) Jaque, D.; Ramirez, O.; Bausá, E.; Solé, G.; Cavalli, E.;  
1011 Speghini, A.; Bettinelli, M. Nd<sup>3+</sup>→Yb<sup>3+</sup> Energy Transfer in the  
1012 YAl<sub>3</sub>(BO<sub>3</sub>)<sub>4</sub> Nonlinear Laser Crystal. *Phys. Rev. B* **2003**, *68* (11), 1–9.
- (41) Trannoy, V.; Carneiro Neto, A. N.; Brites, C. D. S.; Carlos, L. D.;  
Serier-Braut, H. Engineering of Mixed Eu<sup>3+</sup>/Tb<sup>3+</sup> Metal–Organic  
Frameworks Luminescent Thermometers with Tunable Sensitivity. *Adv. Opt. Mater.* **2021**, *9* (6), 2001938.
- (42) Lupei, A.; Lupei, V.; Ikesue, A.; Gheorghe, C.; Hau, S. Nd →  
Yb Energy Transfer in (Nd, Yb): Y<sub>2</sub>O<sub>3</sub> Transparent Ceramics. *Opt. Mater.* **2010**, *32* (10), 1333–1336.
- (43) Artizzu, F.; Serpe, A.; Marchiò, L.; Saba, M.; Mura, A.; Mercuri,  
M. L.; Bongiovanni, G.; Deplano, P.; Quochi, F. Controlling Nd-to-  
Yb Energy Transfer through a Molecular Approach. *J. Mater. Chem. C*  
**2015**, *3* (43), 11524–11530.
- (44) Lupei, A.; Lupei, V.; Ikesue, A.; Gheorghe, C. Spectroscopic  
and Energy Transfer Investigation of Nd/Yb in Y<sub>2</sub>O<sub>3</sub> Transparent  
Ceramics. *J. Opt. Soc. Am. B* **2010**, *27* (5), 1002–1010.
- (45) Balda, R.; Peña, J. I.; Arriandiaga, M. A.; Fernández, J. Efficient  
Nd<sup>3+</sup>→Yb<sup>3+</sup> Energy Transfer in 0.8CaSiO<sub>3</sub>·0.2Ca<sub>3</sub>(PO<sub>4</sub>)<sub>2</sub> Eutectic  
Glass. *Opt. Express* **2010**, *18* (13), 13842.
- (46) Yue, D.; Zhang, J.; Zhao, D.; Lian, X.; Cui, Y.; Yang, Y.; Qian,  
G. Ratiometric near Infrared Luminescent Thermometer Based on  
Lanthanide Metal–Organic Frameworks. *J. Solid State Chem.* **2016**,  
*241*, 99–104.
- (47) Guan, M.; Mei, L.; Huang, Z.; Yang, C.; Guo, Q.; Xia, Z.  
Synthesis and Near-Infrared Luminescence Properties of LaOCl:  
Nd<sup>3+</sup>/Yb<sup>3+</sup>. *Infrared Phys. Technol.* **2013**, *60*, 98–102.
- (48) Liu, J.; Pei, L.; Xia, Z.; Xu, Y. Hierarchical Accordion-like  
Lanthanide-Based Metal–Organic Frameworks: Solvent-Free Syn-  
theses and Ratiometric Luminescence Temperature-Sensing Prop-  
erties. *Cryst. Growth Des.* **2019**, *19* (11), 6586–6591.
- (49) Ying, P.; Yu, J.; Su, W. Liquid-Assisted Grinding Mecha-  
nochemistry in the Synthesis of Pharmaceuticals. *Adv. Synth. Catal.*  
**2021**, *363* (5), 1246–1271.
- (50) Kosimov, A.; Yusibova, G.; Aruväli, J.; Paiste, P.; Käärrik, M.;  
Leis, J.; Kikas, A.; Kisand, V.; Šmits, K.; Kongi, N. Liquid-Assisted  
Grinding/Compression: A Facile Mechanochemical Route for the  
Production of High-Performing Co–N–C Electrocatalyst Materials.  
*Green Chem.* **2022**, *24* (1), 305–314.
- (51) Friščić, T.; Halasz, I.; Štrukil, V.; Eckert-Maksić, M.; Dinnebier,  
R. E. Clean and Efficient Synthesis Using Mechanochemistry:  
Coordination Polymers, Metal–Organic Frameworks and Metal-  
lodrugs. *Croat. Chem. Acta* **2012**, *85* (3), 367–378.
- (52) Davies, K.; Bourne, S. A.; Oliver, C. L. Solvent- and Vapor-  
Mediated Solid-State Transformations in 1,3,5- Benzenetricarboxylate  
Metal – Organic Frameworks. *Cryst. Growth Des.* **2012**, *12*, 1999–  
2003.
- (53) Biradha, K.; Ramanan, A.; Vittal, J. J. Coordination Polymers  
Versus Metal–Organic Frameworks. *Cryst. Growth Des.* **2009**, *9* (7),  
2969–2970.
- (54) Steed, J. W.; Atwood, J. L. *Supramolecular Chemistry*, 2nd ed.;  
Wiley: Chichester, UK, 2009.
- (55) Mahalakshmi, G.; Balachandran, V. FT-IR and FT-Raman  
Spectra, Normal Coordinate Analysis and Ab Initio Computations of  
Trimesic Acid. *Spectrochim. Acta, Part A* **2014**, *124*, 535–547.
- (56) Deacon, G. B.; Phillips, R. J. Relationships between the  
Carbon-Oxygen Stretching Frequencies of Carboxylate Complexes  
and the Type of Carboxylate Coordination. *Coord. Chem. Rev.* **1980**,  
*33* (3), 227–250.
- (57) Kerim, F. M. A.; Aly, H. F.; El-Agramy, A. Infrared Absorption  
Spectra of Some Lanthanide Acetylacetonate Complexes. *Proc. Indian  
Acad. Sci.* **1977**, *85* (6), 559–566.
- (58) Sahiner, N.; Demirci, S.; Yildiz, M. Preparation and  
Characterization of Bi-Metallic and Tri-Metallic Metal Organic  
Frameworks Based on Trimesic Acid and Co(II), Ni(II), and Cu(II)  
Ions. *J. Electron. Mater.* **2017**, *46* (2), 790–801.
- (59) Sel, K.; Demirci, S.; Meydan, E.; Yildiz, S.; Ozturk, O. F.; Al-  
Lohedan, H.; Sahiner, N. Benign Preparation of Metal–Organic  
Frameworks of Trimesic Acid and Cu, Co or Ni for Potential Sensor  
Applications. *J. Electron. Mater.* **2015**, *44* (1), 136–143.
- (60) Feng, W.; Zhang, Y.; Zhang, Z.; Su, P.; Lü, X.; Song, J.; Fan, D.;  
Wong, W. K.; Jones, R. A.; Su, C. Near-Infrared (NIR) Luminescent



- 1082 Metallopolymers Based on Ln 4(Salen)<sub>4</sub> Nanoclusters (Ln = Nd or 1083 Yb). *J. Mater. Chem. C* **2014**, *2* (8), 1489.
- 1084 (61) Carnall, W. T. The Near-Infrared Transitions of the Trivalent 1085 Lanthanides in Solution. II. Tb<sup>3+</sup>, Dy<sup>3+</sup>, Ho<sup>3+</sup>, Er<sup>3+</sup>, Tm<sup>3+</sup>, and Yb<sup>3+</sup>. *J.* 1086 *Phys. Chem.* **1963**, *67* (6), 1206–1211.
- 1087 (62) Rast, H. E.; Caspers, H. H.; Miller, S. A. Fluorescence and 1088 Energy Transfer between Nd<sup>3+</sup> and Yb<sup>3+</sup> in LaF<sub>3</sub>. *J. Chem. Phys.* **1967**, 1089 *47* (10), 3874–3878.
- 1090 (63) Ryba-Romanowski, W.; Golab, S.; Pisarski, W. A. Investigation 1091 of Infrared-to-Visible Conversion in Cubic Cs<sub>2</sub>NaErCl<sub>6</sub> Crystals. *J.* 1092 *Phys.: Condens. Matter.* **1995**, *7* (37), 7397–7404.
- 1093 (64) Carneiro Neto, A. N.; Moura, R. T.; Malta, O. L. On the 1094 Mechanisms of Non-Radiative Energy Transfer between Lanthanide 1095 Ions: Centrosymmetric Systems. *J. Lumin.* **2019**, *210*, 342–347.
- 1096 (65) Padlyak, B. V.; Ryba-Romanowski, W.; Lisiecki, R.; Oseledchik, 1097 Y. S.; Prosvirnin, A. L.; Kudryavtsev, D. P.; Svitanko, N. V. Optical 1098 Spectroscopy of the Nd<sup>3+</sup> Luminescence Centres in the Sr<sub>4</sub>B<sub>14</sub>O<sub>25</sub>: Nd 1099 Crystal. *Acta Phys. Polym., A* **2010**, *117* (1), 104–110.
- 1100 (66) Meijerink, A.; Blasse, G.; Sytsma, J.; Ellens, A. Electron— 1101 Phonon Coupling in Rare Earth Compounds. *ACTA Phys. Polym., A* 1102 **1996**, *90* (1), 109–119.
- 1103 (67) Karbowski, M.; Sobczyk, M.; Drożdżyński, J. Comparison 1104 between Electron–Phonon Coupling Strengths of U<sup>3+</sup> and Nd<sup>3+</sup> Ions 1105 Doped in LaCl<sub>3</sub> and U<sup>3+</sup> in LaBr<sub>3</sub> Single Crystals. *J. Solid State Chem.* 1106 **2003**, *173* (1), 59–68.
- 1107 (68) Kushida, T. Energy Transfer and Cooperative Optical 1108 Transitions in Rare-Earth Doped Inorganic Materials. I. Transition 1109 Probability Calculation. *J. Phys. Soc. Jpn.* **1973**, *34* (5), 1318–1326.
- 1110 (69) Malta, O. L. Mechanisms of Non-Radiative Energy Transfer 1111 Involving Lanthanide Ions Revisited. *J. Non-Cryst. Solids* **2008**, *354* 1112 (42–44), 4770–4776.
- 1113 (70) Judd, B. R. Optical Absorption Intensities of Rare-Earth Ions. 1114 *Phys. Rev.* **1962**, *127* (3), 750–761.
- 1115 (71) Ofelt, G. S. Intensities of Crystal Spectra of Rare-Earth Ions. *J.* 1116 *Chem. Phys.* **1962**, *37* (3), 511–520.
- 1117 (72) Qin, X.; Carneiro Neto, A. N.; Longo, R. L.; Wu, Y.; Malta, O. 1118 L.; Liu, X. Surface Plasmon–Photon Coupling in Lanthanide-Doped 1119 Nanoparticles. *J. Phys. Chem. Lett.* **2021**, *12* (5), 1520–1541.
- 1120 (73) Butcher, J. C. Numerical Methods for Ordinary Differential 1121 Equations in the 20th Century. *J. Comput. Appl. Math.* **2000**, *125* (1– 1122 2), 1–29.
- 1123 (74) Hairer, E.; Wanner, G. Radau Methods. In *Encyclopedia of* 1124 *Applied and Computational Mathematics*, Engquist, B.; Springer: 1125 Berlin, Heidelberg, 2015; pp. 12131216. .
- 1126 (75) Fang, M.; Neto, A. N. C.; Fu, L.; Ferreira, R. A. S.; de Zea 1127 Bermudez, V.; Carlos, L. D. A Hybrid Materials Approach for 1128 Fabricating Efficient WLEDs Based on Di-Ureasils Doped with 1129 Carbon Dots and a Europium Complex. *Adv. Mater. Technol.* **2022**, *7* 1130 (3), 2100727.
- 1131 (76) Mamontova, E.; Botas, A. M. P.; Brites, C. D. S.; Ferreira, R. A. 1132 S.; Rouquette, J.; Guari, Y.; Larionova, J.; Long, J.; Carlos, L. D. 1133 Rationalizing the Thermal Response of Dual-Center Molecular 1134 Thermometers: The Example of an Eu/Tb Coordination Complex. 1135 *Adv. Opt. Mater.* **2022**, *10* (5), 2101870.
- 1136 (77) Ramalho, J. F. C. B.; Dias, L. M. S.; Fu, L.; Botas, A. M. P.; 1137 Carlos, L. D.; Carneiro Neto, A. N.; André, P. S.; Ferreira, R. A. S. 1138 Customized Luminescent Multiplexed Quick-Response Codes as 1139 Reliable Temperature Mobile Optical Sensors for EHealth and 1140 Internet of Things. *Adv. Photonics Res.* **2022**, *3*, 2100206.
- 1141 (78) Ramalho, J. F. C. B.; Carneiro Neto, A. N.; Carlos, L. D.; 1142 André, P. S.; Ferreira, R. A. S. Lanthanides for the New Generation of 1143 Optical Sensing and Internet of Things. In *Handbook on the Physics* 1144 *and Chemistry of Rare Earths*, Bünzli, J.-C. G.; Pecharsky, V. K., Eds.; 1145 Elsevier, 2022, pp. 31128.
- 1146 (79) Kasprzycka, E.; Carneiro Neto, A. N.; Trush, V. A.; Malta, O. 1147 L.; Jerzykiewicz, L.; Amirkhanov, V. M.; Legendziewicz, J.; 1148 Gawryszewska, P. Spectroscopic Aspects for the Yb<sup>3+</sup> Coordination 1149 Compound with a Large Energy Gap between the Ligand and Yb<sup>3+</sup> 1150 Excited States. *Spectrochim. Acta, Part A* **2022**, *274*, 121072.
- (80) Lyubov, D. M.; Carneiro Neto, A. N.; Fayoumi, A.; Lyssenko, 1151 K. A.; Korshunov, V. M.; Taydakov, I. V.; Salles, F.; Guari, Y.; 1152 Larionova, J.; Carlos, L. D.; et al. Employing Three-Blade 1153 Propeller Lanthanide Complexes as Molecular Luminescent Ther- 1154 mometers: Study of Temperature Sensing through a Concerted 1155 Experimental/Theory Approach. *J. Mater. Chem. C* **2022**, *10* (18), 1156 7176–7188. 1157
- (81) Salerno, E. V.; Carneiro Neto, A. N.; Eliseeva, S. V.; 1158 Hernández-Rodríguez, M. A.; Lutter, J. C.; Lathion, T.; Kampf, J. 1159 W.; Petoud, S.; Carlos, L. D.; Pecoraro, V. L. Tunable Optical 1160 Molecular Thermometers Based on Metallacrowns. *J. Am. Chem. Soc.* 1161 **2022**, *144* (40), 18259–18271. 1162
- (82) Moura Jr, R. T.; Carneiro Neto, A. N.; Longo, R. L.; Malta, O. 1163 L. On the Calculation and Interpretation of Covalency in the Intensity 1164 Parameters of 4f-4f Transitions in Eu<sup>3+</sup> Complexes Based on the 1165 Chemical Bond Overlap Polarizability. *J. Lumin.* **2016**, *170*, 420–430. 1166
- (83) Malta, O. L. A Simple Overlap Model in Lanthanide Crystal- 1167 Field Theory. *Chem. Phys. Lett.* **1982**, *87* (1), 27–29. 1168
- (84) Miyakawa, T.; Dexter, D. L. Phonon Sidebands Multiphonon 1169 Relaxation of Excited States, and Phonon-Assisted Energy Transfer 1170 between Ions in Solids. *Phys. Rev. B* **1970**, *1* (7), 2961–2969. 1171
- (85) Grant, W. J. C. Role of Rate Equations in the Theory of 1172 Luminescent Energy Transfer. *Phys. Rev. B* **1971**, *4* (2), 648–663. 1173
- (86) Ferreira, R. A. S.; Carneiro Neto, A. N.; Correia, S. F. H.; 1174 Carlos, L. D. Lanthanide Emission for Solar Spectral Converters: An 1175 Energy Transfer Viewpoint. In *Springer Series on Fluorescence*; 1176 Springer: Cham, 2021; pp. 133. DOI: . 1177
- (87) Carneiro Neto, A. N.; Teotonio, E. E. S.; de Sá, G. F.; Brito, H. 1178 F.; Legendziewicz, J.; Carlos, L. D.; Felinto, M. C. F. C.; 1179 Gawryszewska, P.; Moura Jr, R. T.; Longo, R. L.; Faustino, W. M.; 1180 Malta, O. L. Modeling Intramolecular Energy Transfer in Lanthanide 1181 Chelates: A Critical Review and Recent Advances. In *Handbook on the* 1182 *Physics and Chemistry of Rare Earths*, Bünzli, J.-C. G.; Pecharsky, V. K., 1183 Eds.; Elsevier, 2019; Vol. 56, pp. 55162. DOI: . 1184
- (88) Blois, L.; Malta, O. L.; Brito, H. F. The Role of the Eu<sup>3+</sup> 1185 <sup>5</sup>D<sub>0</sub> Emitting Level through the Direct Sensitization of the <sup>5</sup>D<sub>0</sub> 1186 Emitting Level through Intramolecular Energy Transfer. *J. Lumin.* **2022**, *247*, 118862. 1187